Blind Deconvolution of Anisoplanatic Aberrations

a computational correction of microscopic images

W. van de Ketterij

Master of Science Thesis

TU Delft Delft University of Technology

Delft Center for Systems and Control

Blind Deconvolution of Anisoplanatic Aberrations

a computational correction of microscopic images

Master of Science Thesis

W. van de Ketterij

June 25, 2019

Faculty of Mechanical, Maritime and Materials Engineering (3mE) · Delft University of Technology

Abstract

Diversity in the distribution of the refractive index in biological samples causes phase aberrations in imaging systems [1, 2]. These phase aberrations will result in degradation of the image quality. Post processing algorithms try to reconstruct the object from the obtained images.

Correction techniques, such as tangential iterative projections (TIP) [3], were developed to reconstruct the image for the whole field of view. However, due to the three dimensional nature of biological tissues, induced aberrations are different throughout the field of view. This Master of Science thesis shows the development of four algorithms. These algorithms apply TIP to deconvolve images locally. Thereafter, the local results are combined in order to restore images from anisoplanatic aberrations. The difference between the the algorithms developed during this research is the complexity in the spatial domain and in the Fourier domain. It was found that adaptive limited support in the spatial domain increases the image quality of the estimated object. A novel approach for multi-frame deconvolution in the Fourier domain has shown to be a promising modification. The use of weighted multi-frame deconvolution in the Fourier domain has lead to improved image quality.

During the research it was found that some image quality metrics, such as Fourier ring correlation and structural similarity, are useful to show the performance of an image restoration algorithm. Moreover, it was discovered that metrics based around the mean square error are less useful to compare performance in situations where aberrations are anisoplanatic.

The goal and motivation of this thesis is to contribute to the accessibility of imaging system. Computational imaging is the joint design of both imaging systems and processing algorithms. The aim of these algorithms is to reconstruct an object and correct for aberrations induced by the sample or the imaging system. Nowadays computing power is cheaper than good optical components. Computational imaging is capable of designing cheap portable microscopes which can be applied in the field to do disease diagnoses for example.

Table of Contents

List of Figures

List of Tables

Preface

This document is a part of my Master of Science graduation thesis. The idea of doing my thesis on this subject came during prof. dr. ir. M. Verhaegen's lectures. He mentioned the ability to correct for imperfections in low cost imaging systems. He inspired me to elect courses in the field of imaging and doing my thesis in Computational Imaging. I decided to do my research on computational approaches to aberration correction, because of the involved mathematics. My passion for mathematics has always been the motivation for studying in general. It provides understanding to complex problems and challenges me to come up with solutions. Besides mathematics, it is biology, physics and ethics that help me to appreciate life and inspired me to make the world a better place.

This Master of Science thesis shows the development of four new algorithms. These algorithms are designed to handle anisoplanatic aberrations. This thesis will contribute to the field of computational imaging. By these means I hope to participate in a broader research in the field of disease diagnoses.

This thesis is written for readers who are interested in the field of Computational Imaging, Adaptive Optics, Systems and Control and Signal processing. Chapter 1, Introduction, describes the main problem, aim and outline of this literature survey. Chapters 2 - 6 cover work that was done in thesis. Finally Chapter 7 concludes the work. This last chapter also discusses the next step in this research.

Delft, University of Technology — W. van de Ketterij
June 25, 2019

Acknowledgements

I would like to thank my supervisor prof. dr. ir. M. Verhaegen for his assistance during the writing of this thesis. Thank you for learning me how to focus on the subject and how to formulate clear objectives. Your supervision helped in creating this literature survey. Your critical standpoint motivated me think hard and explain new insights in a clear and understandable way for everyone.

I would like to thank dr. O. A. Soloviev for his weekly guidance. Special thanks to the motivating lectures about wave numbers, the Fourier transform and more. Thank you for providing me with interesting papers and introducing me to inspiring authors. Discussing how to read articles, papers and other document helped me and learned me how to process information efficiently.

I would like to thank dr. C. Smith for introducing me to FRC. FRC is a metric for image quality that was used frequently during this thesis.

I would like to acknowledge the support of family and friends for their interest in my progression during this year.

Delft, University of Technology W. van de Ketterij
June 25, 2019

"Wit beyond measure is man's greatest treasure."
— *J.K. Rowling*

Chapter 1

Introduction

1-1 Problem Description

Microscopes are one of the most important tools in biological research and human understanding of diseases. However, the ability of microscopes to investigate processes inside biological tissue is limited. It is only possible to see into most biological tissues up to approximately a hundred microns. Due to the inhomogeneous distribution of refractive index in biological tissue light is deflected. Because of these deflections light has to travel more distance than trough vacuum. Since this deviation in path length dependents on the refractive index, the deviations differ trough the field of view (FOV). Therefore it is necessary to compute the unique correction for every point in the image [2].

Wu and Cui [13] show that widely adopted isoplanatic correction for a phase aberration in the pupil plane is outperformed by the multi-conjugate correction methods. For a small FOV the single-conjugation correction nearly doubles the peak intensity compared to the isoplanatic correction. Wu and Cui conclude that the isoplanatic pupil plane correction should be used to handle spatially invariant wavefront distortions, and that the conjugation plane should be used to correct for anisoplanatic phase aberrations.

Wilding *et al.* [3] present the tangential iterative projections (TIP) algorithm to perform the isoplanatic pupil plane correction in imaging scenarios where temporal variation of the phase aberration occur. This Master of Science thesis takes spacial variation or the three dimensional nature of the problem into account. In deep tissue microscopy anisoplanatic phase aberrations occur and therefore it is necessary to apply a correction method that can handle these variations.

1-2 Aim of the Research

Research was conducted to design an algorithm that is able to perform a correction for anisoplanatically deteriorated images. This is the case in deep tissue microscopy. The aim of this research is to expand theoretical knowledge in literature about computational correction methods. Furthermore it is desirable to design an algorithm that outperforms similar state-of-the-art algorithms. In order to achieve this design the problem was divided into smaller problems. First, image deterioration is studied in order to understand why images are degraded and what models can be used to describe this phenomenon mathematically. Secondly, other computation correction algorithms are studied. New insight can lead to improvement of current state-of-the-art algorithms or can even lead to the development of a new algorithm. Thirdly, a metric must be chosen such that different approaches can be compared quantitatively. Finally the performance of the algorithm will be evaluated in experiments. Simulations with empirical data and real data will be conducted and the performance of the algorithm will be compared to another algorithm.

1-3 Outline

In order to understand the physics behind optical systems and the correction methods this thesis starts with a brief introduction to imaging. In Chapter 2, some basic optical concepts are introduced and the reader becomes familiar with terminology. Chapter 2 covers the formation of images in the presence of a phase aberration. Chapter 3 is dedicated to correction methods known in literature. First correction methods for isoplanatic aberrations are discussed. These isoplanatic methods form the basis for the correction of anisoplanatic phase aberrations. In the last part of Chapter 3, efficient image models for anisoplanatic correction methods are presented and a correction framework is described. Chapter 4 describes the development of the first algorithm called TIP3A. It provides the reader with a detailed description of the algorithm. In Chapter 5 is discussed what image metric represents the image quality the best. This metric will be used throughout the thesis to compare the convergence and performance of the algorithms. Chapter 6 shows that improvements to the first algorithm can be made. Improvements in the spatial domain and Fourier domain lead to the development of three other algorithms. The end of Chapter 6 demonstrates the performance of the algorithm, TIP4A-W, when much noise is present in the images. This algorithm is also tested on real images and compared to another algorithm. Chapter 7 is the final chapter. Chapter 7 will conclude the work and formulate a future outlook.

Chapter 2

Image formation and deterioration in Fourier Optics

Light can be used to gather information of a scientific object. This chapter provides mathematical models for the image of a point source and models for deteriorated images of an extended object. This knowledge is required to understand the way images are formed and deteriorated, such that a correction method can be developed. This chapter has two sections. In the first section, some basic optical concepts are explained. The reader is introduced to wavefronts, the wave-like nature of light the image of a point source. In the second section the formation and degradation of images of an extended object is described.

2-1 Image of a Point Source in Fourier Optics

A point source emits light in all direction. When this light is captured by an imaging system to form an image, it will not be a perfect point. The wave-like nature of light, or electromagnetic radiation, will cause deterioration of an image. Moreover, if light waves travel trough imperfect medium the image quality will decrease further.

2-1-1 Basic Optical Concepts

The Maxwell's equations are derived from basic concepts in electricity and magnetism. From the Maxwell's equations in vacuum can be shown [14, 15] that each Cartesian component of electric field and magnetic field must satisfy the three-dimensional *scalar* wave equation,

$$\nabla^2 u = \frac{1}{\nu^2}\frac{\partial^2 u}{\partial t^2}, \tag{2-1}$$

where, $\nu = (\mu_0\epsilon_0)^{-\frac{1}{2}}$, equal to the speed of light c.

With the current hardware, it is not possible to detect the temporal fluctuations of the electromagnetic field [2]. Since the time dependence is known *a priori*, it can be shown [15] that time averaged electromagnetic waves, $U(\boldsymbol{r}) = A(\boldsymbol{r})e^{-i\phi(\boldsymbol{r})}$ at location $\boldsymbol{r} \in \mathbb{R}^3$, must obey the Helmholtz equation:

$$(\nabla^2 + k^2)U = 0 \tag{2-2}$$

Resulting in the following expressions for spherical and plane waves respectively:

$$U_s(\boldsymbol{r}) = \frac{A}{|\boldsymbol{r} - \boldsymbol{r}_0|} e^{-ik|\boldsymbol{r}-\boldsymbol{r}_0| - i\phi_0}, \tag{2-3}$$

$$U_p(\boldsymbol{r}) = Ae^{-i\boldsymbol{k}\cdot\boldsymbol{r} - i\phi_0}. \tag{2-4}$$

Intensity

The energy of a wave is proportional to its amplitude. The intensity, measured by a charge-coupled device (CCD) for example, is given by the amplitude squared of the electromagnetic waves. The intensity of a spherical wave at $\boldsymbol{r}$ is given by

$$I_s(\boldsymbol{r}) = |U_s(\boldsymbol{r})|^2 = \frac{A^2}{|\boldsymbol{r} - \boldsymbol{r}_0|^2}. \tag{2-5}$$

In general, the intensity at a point $\boldsymbol{r}$ is given by the amplitude squared of the electromagnetic waves:

$$I(\boldsymbol{r}) = |U(\boldsymbol{r})|^2 = |A(\boldsymbol{r})|^2. \tag{2-6}$$

Wavefront Aberrations

Imperfections in the shape of optical components or misalignment in imaging systems cause aberrations in the wavefronts. Hence it is almost impossible to reach resolutions close to the refraction limit. Beside these inherent imperfections, imaging systems suffer from external conditions, such as thermal effects, atmospheric turbulence or inhomogeneous medium. Phase aberrations are changes in the wavefront. Since the wavefront is given by a surface of constant phase of a complex electromagnetic wave, $U(\boldsymbol{r}) = A(\boldsymbol{r})e^{-i\phi(\boldsymbol{r})}$, the wavefront distortion or phase aberration is a deviation from the perfect wave shape.

Phase aberrations cause deterioration of images obtained from imaging systems. Therefore, it is of high importance to correct these distorted wavefronts.

Zernike Polynomials

A commonly used method in optics to describe a wavefronts is to represent it as a weighted sum of Zernike Polynomials. Those are predefined functions, called modes. Zernike polynomials are defined for any two non-negative integers of the same parity m, n:

$$m, n \in \mathbb{Z} \geq 0, \qquad n \geq m, \qquad n - m \in 2\mathbb{Z}.$$

Noll [16] (cited in [4]) introduced a different numbering, using a single index for Zernike Polynomials Z_N. Although Zernike polynomials are defined in polar coordinates, their Cartesian representation as given in Figure 2-1 looks very harmless. This figure shows the first

15 Zernike polynomials. Considering Noll's order, the phase, for instance in the pupil plane $z = z_p$, can be represented as:

$$\phi(x, y) = \sum_i a_i Z_i. \tag{2-7}$$

Representing the wavefront in such a way comes with some advantages. First of all, Zernike polynomials are orthogonal on a unit disk. They always reach 1 at the aperture boundary. The main optical aberrations are easily expressed in Zernike polynomials. In order to reduce algorithm stagnation it is often better to estimate low order Zernike polynomials first [17].

2-1-2 The Image of a Point Source

As a result of the thin lens equation, it is known that a lens converts a plane wave onto a spherical wave converging to a point in the focal plane. And the other way around, a spherical wave originating from the focal plane will be converted into a plane wave.

physical optics has shown that a lens performs a Fourier transform. A wave, $ae^{-i\phi(x,y)}$, with aberration, $\phi(x, y)$, at the pupil, will result in a field distribution in the back focal plane

$$A(x, y) \approx \frac{e^{i\frac{2\pi f}{\lambda}} e^{i\frac{\pi}{\lambda f}\left(x^2+y^2\right)}}{i\lambda f} \iint_{\mathbb{R}^2} P(x, y) a e^{-i\phi(x,y)} e^{-i\frac{2\pi}{\lambda f}(x_o x + y_o y)} dx_o dy_o, \tag{2-8}$$

where $P(x, y)$ is called the pupil function. The pupil function is typically 1 inside the lens aperture and 0 outside. f is the focal length of the lens and λ is the wave length. x_o and y_o are the spacial coordinates in the pupil plane.

Point Spread Function

Since the image is given by the intensity of the field distribution, the image of a point source in the far field is given by

$$I(x, y) = \frac{a^2}{\lambda^2 f^2} \left| \iint_{\mathbb{R}^2} P(x, y) e^{-i\phi(x,y)} e^{-i\frac{2\pi}{\lambda f}(x_o x + y_o y)} dx_o dy_o \right|^2. \tag{2-9}$$

This integral can be recognized as a two-dimensional Fourier transform. The point spread function (PSF) of a unit point source can be written as

$$I(x, y) = c \left| \mathcal{F}\left\{ P(x, y) e^{-i\phi(x,y)} \right\} \right|^2, \tag{2-10}$$

where c is a normalization constant. Figure 2-2 shows a normalized intensity distribution for a point source in the far field. This intensity distribution for an imaging system without aberration is diffraction limited. The shape of this intensity distribution is called an Airy disk. The smallest ring around the origin at zero intensity is given by the Rayleigh resolution criterion. The angular distance of this ring is given by $1.22\lambda/D = 1.54 \cdot 10^{-4} rad$. The radius of this ring is given by $1.22\lambda f/D = 7.72 \cdot 10^{-6} m$.

The image of a point source in the far field obtained from an imaging system with an aberration in the pupil will differ from the Airy disk. The last column in Figure 2-1 shows the images for different aberrations. The image of a point source is called the PSF. The PSF does not depend on the position of the point in the object plane.

Index	Noll's ordering	Name	Expression	Shape	PSF
$Z_0^0(x,y)$	1	piston	1		
$Z_1^1(x,y)$	2	tip	x		
$Z_1^{-1}(x,y)$	3	tilt	y		
$Z_2^0(x,y)$	4	defocus	$2x^2+2y^2-1$		
$Z_2^2(x,y)$	5	astigmatism	x^2-y^2		
$Z_2^{-2}(x,y)$	6	astigmatism	$2xy$		
$Z_3^1(x,y)$	7	coma	$3x^3+3y^2x-2x$		
$Z_3^{-1}(x,y)$	8	coma	$3y^3+3x^2y-2y$		
$Z_3^3(x,y)$	9	trefoil	x^3-3xy^2		
$Z_3^{-3}(x,y)$	10	trefoil	$3x^2y-y^3$		
$Z_4^0(x,y)$	11	spherical	$6x^4+12y^2x^2-6x^2+6y^4-6y^2+1$		
$Z_4^2(x,y)$	12		$4x^4-3x^2-4y^4+3y^2$		
$Z_4^{-2}(x,y)$	13		$8yx^3+8y^3x-6yx$		
$Z_4^4(x,y)$	14		$x^4-6y^2x^2+y^4$		
$Z_4^{-4}(x,y)$	15		$4x^3y-4xy^3$		

Figure 2-1: The first 15 Zernike polynomials sorted by Noll's order. The expression is given in Cartesian coordinates, followed by the corresponding shape. For some aberrations the name is given. The last column shows an image of a point source deteriorated by the corresponding aberration. (Source: [4])

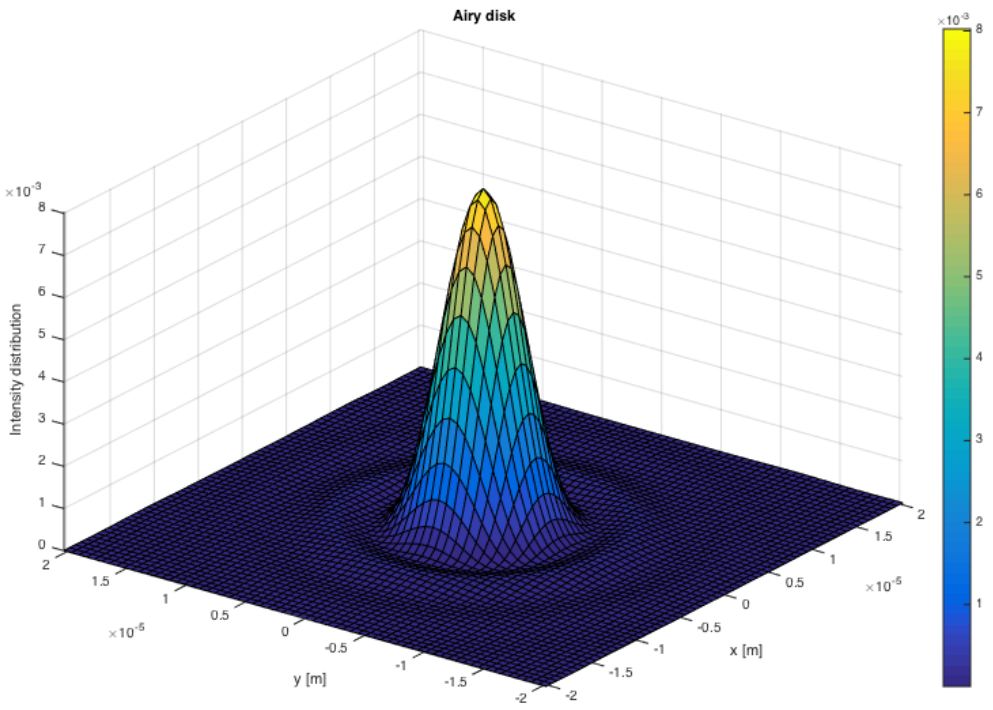

Figure 2-2: The Airy disk is the intensity distribution of a point source in the far field obtained from an imaging system with no aberration. Here the wavelength $\lambda = 633nm$, the lens aperture diameter $D = 5mm$ and the focal length $f = 5cm$.

Resolution of an imaging system

The quality of an imaging system is determined by the width of the PSF. The highest resolution that can be achieved is called the diffraction limit. The Airy disk is the PSF of an imaging system without any aberration. In practise the resolution is lower than the diffraction limit.

Three different measures that characterize the resolution of an imaging system are:

1. Full Width at Half Maximum (FWHM), the width of the PSF at half its maximum intensity.
2. Strehl ratio is the ratio between the peak intensity of the PSF and the peak intensity of the Airy disk.
3. Encircled Energy is the fraction of the total integrated flux in the image contained within a circle of given radius.

2-2 Image of an Extended Object in Fourier Optics

The image of a point source is described by its PSF. However, any two point sources will interfere, so one can only assume the PSF as a space invariant impulse response function, $h(x, y)$, in case of no interference. Assuming incoherent illumination of an extended source, each point in the image is given as a linear super position of the contribution of point sources in the object [2].

$$i(x, y) = \iint_{\mathbb{R}^2} o(\tilde{x}, \tilde{y}) h(x - \tilde{x}, y - \tilde{y}) d\tilde{x} d\tilde{y} = o(x, y) * h(x, y). \tag{2-11}$$

Equation (2-11) is known as the convolution integral. The image of an extended source in incoherent imaging is given by the convolution of the intensity distribution of the object and the incoherent PSF. On the other hand, in case of coherent illumination, image formation is described by the square of convolved field information. For further reading about coherent and incoherent illumination, see Ref. [15]. For the rest of this thesis incoherent illumination is assumed.

2-2-1 Anisoplanatic Phase Aberrations

Aberrations cause image deterioration in microscopy, especially in deep tissue microscopy. It is the three-dimensional nature of biological tissue, where variation in the distribution of the refractive index causes phase aberrations and therefore image degradation [1, 2]. Equation (2-9) shows that the PSF depends on the Fourier transform of the phase aberration, $\phi(x, y)$, inside the pupil. The three-dimensional nature of biological tissue causes the aberrations to differ throughout the field of view (FOV). Therefore, the aberration inside the pupil, $\varphi(x, y|\bar{x}, \bar{y})$, depends on the location of the corresponding point source in the object plane, $o(\bar{x}, \bar{y})$. Aberrations induced outside the pupil plane are referred to as anisoplanatic phase aberrations.

Phase Screen Models

Phase screens or phase masks are used to simulate different distortion layers in imaging systems [13]. A fixed number of two dimensional distortion layers are used to model the effect that three dimensional tissue has on the phase aberrations in the optical system. Wu and Cui [13] simulated this three-dimensional effects by using 96 distortion layers and a Fourier space propagator method to calculate the effect on the wavefront from layer to layer. Simplification of the model allows calculations of the PSF for every pixel from a single phase screen. Figure 2-3 shows an experimental setup where a single phase screen is used outside the pupil plane. A projection method is used to calculate the space-dependent phase aberration, $\varphi(x, y|\bar{x}, \bar{y})$, in the pupil plane.

Phase Aberrations outside the Pupil Plane

Suppose the situation in Figure 2-3. An object is placed at $z_o = l_1 + l_2$ from the pupil plane. In between the object plane and the pupil plane, at distance l_2 from the pupil plane, a phase aberration is induced. The magnitude of the phase aberration is depicted schematically by the black curve in Figure 2-3. In Figure 2-3 can be seen that only a section of the phase aberration in the phase plane has effect on the wavefronts originating from a specific location in the object plane. The object corresponding to the blue optical path passes only through the upper section of the phase plane. It is assumed that the effects of the phase plane can be projected onto the pupil plane, such that the intersection in the phase plane is present inside the pupil. The effect of the phase aberration in the pupil plane for a specific point in the object is given by scaling the intersection between the corresponding optical path and the phase plane. The intersection is scaled in the x and y direction to fit exactly inside the pupil. This projection method allows the use of Equation (2-9) to calculate the PSF.

In this thesis the phase screen model with single phase screen and a projection method is used in simulations in order to create sets of input images with anisoplanatic aberrations. Appendices A and C contain a set of input images that were used in experiments to test the performance of some of the algorithms that are covered in this thesis. Since the phase screen is continuous, the space-dependant phase aberration in the pupil plane is also continuous. This insights is one of the motivations for the development of the TIP3A algorithm in Chapter 4. Explicit use of this phase screen model was not used during the development or design of new algorithms. Explicit use of a phase screen model would require an extra phase retrieval step in the algorithm. This is a potential direction for future research. More information is given in Chapter 6 and in the future outlook in Chapter 7.

Spatially Dependent Point Spread Function

Since every point in the object plane has a corresponding phase aberration in the pupil plane, the PSF for every point can be calculated separately by Equation (2-9). Let the phase screen be given by $\phi(x, y)$ and the projected phase screen in pupil plane is given by $\varphi(x, y|\tilde{x}, \tilde{y})$. The intensity distribution of for the space-variant (SV) PSF is then

$$h(x, y|\tilde{x}, \tilde{y}) = c(\tilde{x}, \tilde{y}) \left| \mathcal{F}\{P(x, y)e^{-i\varphi(x,y|\tilde{x},\tilde{y})}\} \right|^2, \tag{2-12}$$

where $c(\tilde{x}, \tilde{y})$ is proportionality constant such that $\iint_{\mathbb{R}^2} h(x, y|\tilde{x}, \tilde{y})dxdy = 1$.

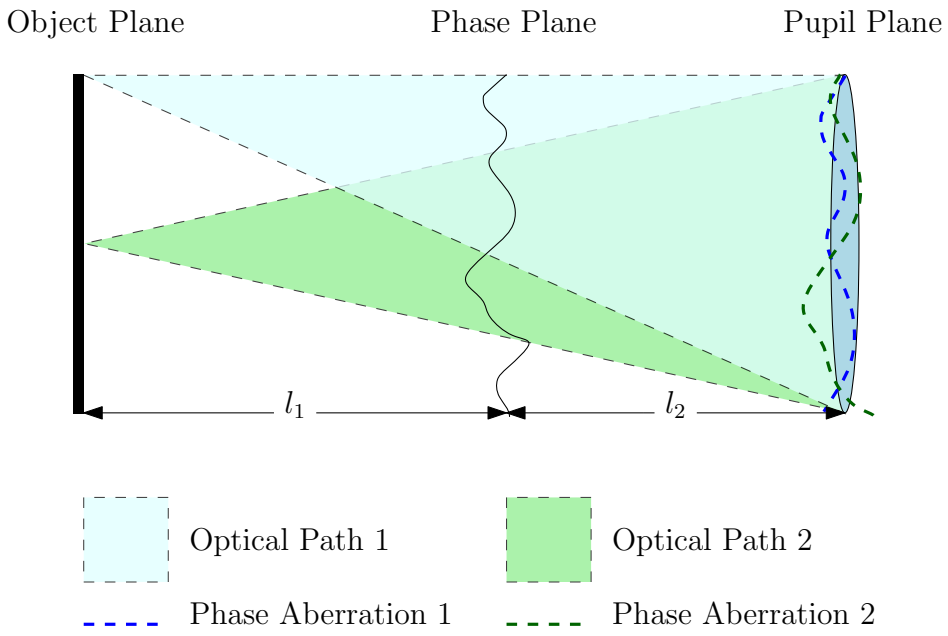

Figure 2-3: A phase aberration induced outside the pupil plane is projected onto the pupil plane. The space-variant point spread function can be calculated from the projected phase aberration inside the pupil. For every point in the object the phase aberration in the pupil plane is the intersection of the phase plane and the optical path corresponding to that point in the object. This intersection is scaled in the x and y direction to be exactly inside the pupil. This figure shows the projected phase aberration for two points in the object.

2-2-2 Anisoplanatic Image Formation

For an incoherent imaging system the image is formed from the contribution of all point sources in the object. Equation (2-12) shows the contribution of a point source with unit intensity. Therefore the total contribution of all point sources, or image, can be written as [18, 19]

$$i(x,y) = \iint_{\mathbb{R}^2} o(\tilde{x},\tilde{y})\tilde{h}(x,y|\tilde{x},\tilde{y})d\tilde{x}d\tilde{y}, \tag{2-13}$$

where $\tilde{h}(x,y|\tilde{x},\tilde{y}) = h(x-\tilde{x},y-\tilde{y}|\tilde{x},\tilde{y})$ are shifted PSFs to match their corresponding object location. Moreover, an image is generally sampled discretely by an imaging sensor, such as a CCD. Let $i_{n,m} \in \mathbb{R}^{N\times N}$ be a discrete N by N image. Then $i_{n,m}$ can be written as

$$i_{n,m} = \sum_{k=1}^{N}\sum_{l=1}^{N} o_{k,l}\tilde{h}_{n,m,k,l}, \qquad n,m,k,l = 1,2,...,N, \tag{2-14}$$

where $o_{k,l} \in \mathbb{R}^{N\times N}$ and $\tilde{h}_{n,m,k,l} \in \mathbb{R}^{N\times N\times N\times N}$ are the discrete samples of the object and SV PSF respectively.

Equation (2-14) can be formulated as convolution in four dimensions. An approach where this 4D convolution is used was researched for this thesis, information about this research can be found in Appendix D.

Effects of Anisoplanatic Phase Aberrations

The left picture in Figure 2-4 shows a picture of the object that was used in a simulation to show the effects of SV PSF on image deterioration. This simulation was conducted for an imaging system with numerical aperture $NA = 0.7$. The phase screen was placed at $l_1 = 0.2z_o$, according to the notation used in Figure 2-3. Furthermore, the phase screen was created by addition of the first 40 Zernike polynomials with random coefficients $-1 \leq a_N \leq 1$, and scaled by an amplitude of 90

$$\phi(x,y) = 90\sum_{N=4}^{40} a_N Z_N. \tag{2-15}$$

Piston, tip and tilt are neglected, as they increase translations in the SV PSF. The amplitude of 90 was chosen to reach sufficient degradation in the obtained images. Figure 2-5 shows the phase screen that was used for the simulation. In order to compare the effects of anisoplanatic aberrations outside the pupil plane with isoplanatic aberrations inside the pupil, the same phase screen was used. However, for the anisoplanatic aberration the phase screen was placed at $l_1 = 0.2z_o$ and projected into the pupil plane for every pixel independently, while for the isoplanatic aberration the projection with respect to the centre of the object was used.

The picture in the right in Figure 2-4 is blurred due to an isoplanatic aberration. It is clear that the image is blurred. The middle picture is degraded by a SV PSF, i.e., All pixels are blurred individually. On top of the SV blur, points in the image are translated individually. This leads to morph of the image. Figure 2-6 shows the PSFs of 49 uniformly placed point sources. The phase screen as shown in Figure 2-5 was used for this simulation. In Figure 2-6

Figure 2-4: The picture on the left shows the non-degraded object. The middle picture shows the degraded object due to a phase screen at $0.2z_o$ in front of the object. The phase screen used during the simulation is depicted in Figure 2-5 and the numerical aperture, $NA = 0.7$. The picture on the right shows the degraded object due to the same phase screen. However, for the middle picture the phase screen was projected onto the pupil plane for every pixel independently, while for the picture in the right the phase screen was projected onto the pupil plane with respect to the centre of the object. This was done to compare the effects of anisoplanatic aberrations with isoplanatic aberrations. The amplitude of the aberration was chosen sufficiently large to demonstrate the effects of anisoplanatic aberrations.

can be seen that the PSFs are spatially dependent and that they are translated. The red crosses show the locations of the point sources. Anisoplanatic aberrations cause SV blur and morph in the obtained image. As a result, every pixel has to be corrected individually to reach high image quality.

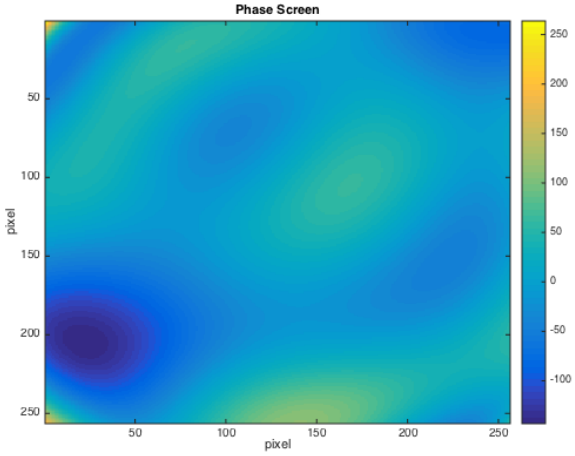

Figure 2-5: This phase screen was obtained from the summation of the first 40 Zernike polynomials, neglecting piston, tip and tilt, $\phi(x,y) = 90\sum_{N=4}^{40} a_N Z_N$. The coefficients a_N are randomly chosen on the interval $[-1,1]$ and the amplitude was chosen to achieve sufficient image deterioration.

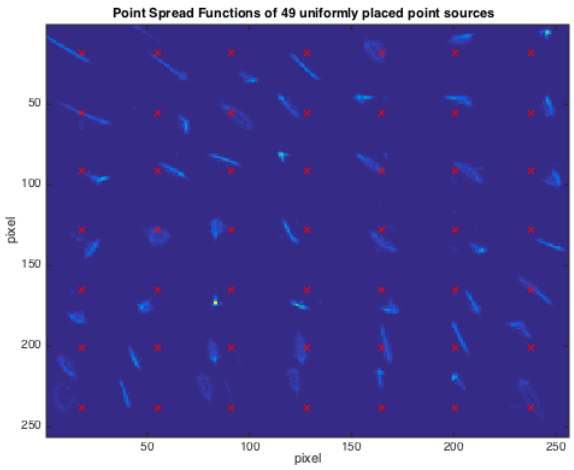

Figure 2-6: 49 point sources are placed uniformly. The locations of the point sources is indicated by the red crosses. It can be seen that the point spread functions are dependent on their spatial location. All point spread functions are individually calculated. They are different from shape and each point spread function is translated individually. This results in space-variant blur and morph of the image.

Chapter 3

Methods in Literature for Correcting Space Invariant and Space-Variant Blur

The effects of induced aberrations outside the pupil plane cause deterioration of images by a space-variant (SV) point spread function (PSF). The first section reviews some widely used devolution methods for known space invariant PSFs. A method is demonstrated that can estimate the object for a given set of images for which the PSFs are unknown. The second section reviews computationally efficient models for SV PSFs. In order to correct for the SV PSF, these efficient models are combined with isoplanatic, or space invariant, correction methods.

3-1 Correction Methods

Numerous correction methods have been developed in order to improve image quality. Although, this research aims at computational methods to correct images, physical correction methods are widely used. In general, adaptive optical systems use a sensor, corrector and a controller. A pupil plane wavefront sensors, such as the shack-Hartman sensor, is used to determine the wavefront. A controller calculates the optimal corrector input. A phase modulator, most often a deformable and reflective surface, is used to correct aberrations in the wavefront. Other methods use a focal plane sensor and the optimization of a non-convex metric in order to calculate the optimal input to the corrector [20].

Physical correction methods try to correct for aberrations in the wavefront. In other words, physical methods optimize the PSF. On the other hand, computational methods work with the imperfect PSFs and apply inverse filters to perform the correction.

3-1-1 Isoplanatic Correction Methods

Equation (2-14) describes the formation of images with anisoplanatic aberration. In practice there is some model mismatch and measurement noise. A general model for image formation is given by

$$i_{n,m} = \sum_{k=1}^{N}\sum_{l=1}^{N} o_{k,l}\tilde{h}_{n,m,k,l} + e_{n,m}, \qquad n,m,k,l = 1,2,...,N, \tag{3-1}$$

where $e_{n,m}$ contains the noise and model mismatch. This model for image formation takes the anisoplanatic aberration into account. Often in literature the PSF can be assumed to be space invariant. Taking only an isoplanatic aberration into account, Equation (3-1) can be written as a discrete convolution and noise,

$$i_{n,m} = \sum_{k=1}^{N}\sum_{l=1}^{N} o_{k,l}h_{n-k,m-l} + e_{n,m}, \qquad n,m,k,l = 1,2,...,N. \tag{3-2}$$

The discrete convolution in Equation (3-2) is denoted by $i_{n,m} = o_{n,m} * h_{n,m} + e_{n,m}$. An advantage of this isoplanatic model is the applicability of the convolution theorem. In the spatial frequency domain, the convolution in Equation (3-2) becomes a point-wise multiplication

$$I_{n,m} = O_{n,m} \times H_{n,m} + E_{n,m}. \tag{3-3}$$

where the capital letter describes the two dimensional discrete Fourier transform, $I_{n,m} = \mathcal{F}\{i_{n,m}\} = \sum_{\tilde{n}=0}^{N-1}\sum_{\tilde{m}=0}^{N-1} i_{\tilde{n}+1,\tilde{m}+1}e^{-j2\pi\left(\frac{n\tilde{n}}{N}+\frac{m\tilde{m}}{N}\right)}$. Similar definition holds for the object and the PSF. Equation (3-3) is referred to as the optical transfer function.

Deconvolution with Known Point Spread Function

A naive approach to deconvolution with a known PSF is to perform point-wise division in the spatial frequency domain or Fourier domain [12].

$$\hat{o}_{n,m} = \mathcal{F}^{-1}\left\{\frac{I_{n,m}}{H_{n,m}+\epsilon}\right\}, \tag{3-4}$$

where ϵ is a small constant to avoid division by zero. $\mathcal{F}^{-1}$ is the inverse two dimensional discrete Fourier transform given by $\mathcal{F}^{-1}\{i_{n,m}\} = \frac{1}{N^2}\sum_{\tilde{n}=0}^{N-1}\sum_{\tilde{m}=0}^{N-1} i_{\tilde{n}+1,\tilde{m}+1}e^{j2\pi\left(\frac{n\tilde{n}}{N}+\frac{m\tilde{m}}{N}\right)}$. This approach can be seen as a solution to the least-squares optimization problem,

$$\hat{o}_{n,m} = \arg\min_{o_{n,m}} ||i_{n,m} - o_{n,m} * h_{n,m}||_F^2, \tag{3-5}$$

where $||\cdot||_F$ denotes the Frobenius norm. Unfortunately, naive inverse filtering amplifies the measurement noise. Figure 3-1 shows the results of a simulation wherein some deconvolution methods are compared. Figure 3-1 (a) shows the object that was used during the simulation. In the top right corner of Figure 3-1 (a) the PSF is shown. Convolution of the object and the PSF, results in the image that is shown in Figure 3-1 (b). Besides convolution with a blurring kernel, white Gaussian noise with standard deviation, $\sigma = 10^{-2}$, was added to the image. A point in the image is a number between 0 and 1. This image is deconvolved with

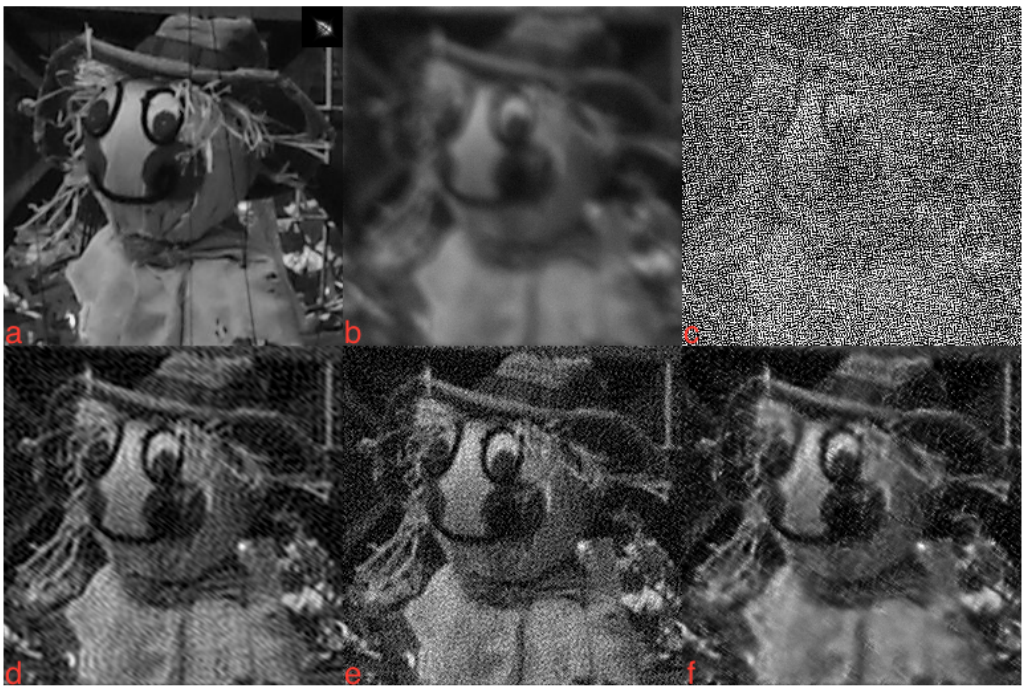

Figure 3-1: The (a) Object and PSF were convolved and white Gaussian noise with standard deviation, $\sigma = 10^{-2}$, was added, resulting in the (b) degraded Image. various deconvolution methods were used to deconvolve the Image with the known PSF. The following methods were used: (c) naive inverse filter, (d) modified naive inverse filter, (e) modified Wiener filter, (f) Richardson-Lucy algorithm. Table 3-1 shows a quantitative comparison between the methods.

the known PSF by four different algorithms. Figure 3-1 (c) is the result of deconvolution by naive inverse filtering (3-4) with $\epsilon = 0.005$.

When a small number, $|H_{n,m}| < \epsilon$, occurs, it will result in a large number in the object's spatial frequency due to the division. However, a zero in $H_{n,m}$ or $O_{n,m}$ should result in a zero in the image $I_{m,n}$. Replacing all elements in $H_{n,m}$ smaller than ϵ by a very large number, will avoid noise amplification. This modified naive inverse filter can be denoted by

$$\hat{o}_{n,m} = \mathcal{F}^{-1}\left\{\frac{I_{n,m}}{H_{n,m}(|H_{n,m}| < \epsilon) = \infty}\right\}, \tag{3-6}$$

where the notation in the denominator describes that point wise division by a complex number, in absolute value smaller than ϵ, is replaced by division by infinity. Figure 3-1 (d) shows the result of deconvolution with known PSF by modified naive inverse filtering (3-6) with $\epsilon = 0.067$. The choice of ϵ is noted in Table 3-1.

Helstrom [21] has shown that an optimum solution in the least-squares sense (3-5) is a Wiener filter of the form

$$\hat{o}_{n,m} = \mathcal{F}^{-1}\left\{\frac{(H_{n,m})^* I_{n,m}}{|H_{n,m}|^2 + \frac{1}{SNR}}\right\}, \tag{3-7}$$

where $H^*_{n,m}$ denotes the complex conjugate of $H_{n,m}$ and SNR is the signal-to-noise ratio. In case the signal-to-noise ratio is unknown a modified Wiener filter [22] (cited in [18]) can be

used.

$$\hat{o}_{n,m} = \mathcal{F}^{-1}\left\{\frac{(H_{n,m})^* I_{n,m}}{|H_{n,m}|^2 + \epsilon}\right\}, \tag{3-8}$$

Figure 3-1 (e) shows the result after deconvolution by the modified Wiener filter with $\epsilon = 0.008$.

Finally, deconvolution by the Richardson-Lucy method will result in Figure 3-1 (f). The Richardson-Lucy algorithm assumes noise following a Poisson distribution. The result is an iterative algorithm that has an optimal number of iterations. This optimum should be set heuristically [12]. A threshold to avoid devising by zero was included, $\epsilon = 0.072$, and the number of iterations was chosen at 63.

$$\hat{o}_{n,m}^{(k+1)} = \hat{o}_{n,m}^{(k)} \times h_{n,m}^T * \frac{i_{n,m}}{\max\{\hat{o}_{n,m}^{(k+1)} * h_{n,m}, \epsilon\}}, \tag{3-9}$$

where $\max\{\cdot\}$, multiplication and division are point-wise. Beside methods that solve the deconvolution problem in the least-squares sense (3-5), there are methods that solve a cost function with additional regularization term, $J(o) = ||i_{n,m} - o_{n,m} * h_{n,m}||^2 + \lambda_o Q(o)$, or similar cost function in the Fourier domain. $||\cdot||$ can denote any matrix norm, most often the Fobenius norm. Methods derived from these cost functions are not shown here. For readers interested in deconvolution with a known PSF, Ref. [12] is recommended.

Table 3-1 shows a quantitative comparison between the deconvolution methods introduced in this section: naive inverse filter, modified naive inverse filter, modified wiener filter and the Richardson-Lucy algorithm. The results in Table 3-1 are obtained from the same experiment as in Figure 3-1. The performance metric that is used is the peak signal-to-noise ratio (PSNR),

$$\text{PSNR} = -10 \log_{10}\left(||o - \hat{o}||_F^2 / N^2\right), \tag{3-10}$$

where o, $\hat{o}$ and N^2 are the object, estimated object and number of pixel respectively. The PSNR is measured in decibels (dB). Since Gaussian noise was used during the experiment, it was expected that the modified Wiener filter performed the best. Within 0.8% difference in performance, the modified naive inverse filter performed second best. The Richardson-Lucy method assumes Poisson noise while Gaussian noise was used during the experiment. For this reason it was expected that the Richardson-Lucy method performs worse than the modified Wiener filter. Lastly, the naive inverse filter has negative performance. The naive inverse filter is known to amplify noise.

Deconvolution with Unknown Point Spread Function

In microscopy of biological samples the aberrations and PSF could be unknown. In blind deconvolution, both the object and the PSF are estimated. There are two main classes of blind deconvolution methods. In the first class of methods the PSF is identified prior to the deconvolution step. Cannon [23] shows that the log power spectrum of the image, $P_i(x, y) = \mathcal{F}\{\log \phi_b(x, y)\}$, contains sufficient information for PSF identification. However, methods of this kind work only to identify simple PSFs [24]. The second and larger class of blind deconvolution methods, contains methods that jointly identify object and PSF. The

Table 3-1: A quantitative comparison between deconvolution methods with known point spread function. The compared deconvolution methods are: naive inverse filter (NIF), modified naive inverse filter (MNIF), modified Wiener filter (MWF) and Richardson-Lucy method (RL). For NIF, $\epsilon = 0.05$ is chosen to be relatively low, as suggested in [12]. The parameter ϵ for the methods MNIF, MWF and RL chosen op optimize the resulting peak signal-to-noise ratio (PSNR). PSNR $= -10\log_{10}\left(||o-\hat{o}||_F^2/N^2\right)$, where o, $\hat{o}$ and N^2 are the object, estimated object and number of pixel respectively. Since the NIF method is known to amplify noise, it is expected to perform the least. MNIF and MWF perform the best. These methods outperform the RL method in this experiment, because Gaussian noise was used. The RL methods performs the best when Poisson noise is used [12]. Performance is measured in terms of PSNR. A visual comparison is shown in Figure 3-1.

Algorithm	**NIF**	**MNIF**	**MWF**	**RL**
ϵ	0.005	0.067	0.008	0.072
PSNR(dB)	-1.16	25.5	25.7	23.8

majority of this class uses an alternating approach. Methods from the second class rely on prior knowledge about the object and PSF [25].

In general these alternating methods that estimate both the object and the PSF can be formulated as regularized least-squares optimization problem [24, 3],

$$\{\hat{h}_{n,m}, \hat{o}_{n,m}\} = \arg\min_{h,o} ||i_{n,m} - o_{n,m} * h_{n,m}||^2 + \lambda_o Q(o) + \lambda_h R(h), \tag{3-11}$$

or a similar cost function in the Fourier domain. For readers interested in methods in this class (3-11), see Ref. [24]. The rest of this chapter demonstrates methods that belong to a subsection of this class. Consider the following least-squares optimization problem.

$$\{\hat{H}_{n,m}, \hat{O}_{n,m}\} = \arg\min_{H,O} ||I_{n,m} - O_{n,m} * H_{n,m}||_F^2. \tag{3-12}$$

This problem is a classic ill-posed inverse problem [3], there are infinite solution to the optimization problem. The infinite set of solutions to this problem contains also trivial solutions such as, $o_{n,m} = i_{n,m}$ and $h_{n,m} = \delta_{n-\tilde{n},m-\tilde{m}}$, where $\delta_{n-\tilde{n},m-\tilde{m}}$ is the discrete Delta function, that is 0 everywhere, but 1 at $n = \tilde{n}$, $m = \tilde{m}$. Convergence of the methods towards the real solution relies on prior knowledge about the object and PSF.

The pioneering work of Gerchberg and Saxton [26] in 1972 demonstrated the use of an alternating projection framework to solve inverse problems. In 1988, Ayers and Dainty [27] applied this alternating projection framework to the deconvolution problem. The algorithm proposed by Ayers and Dainty consists of eight steps that result in an iterative loop. The loop is initialized by a non-negative initial estimate, $\bar{h}_{n,m}^{(0)}$. The kth iteration has the following steps:

- **Step 1:** $\bar{H}_{n,m}^{(k)} = \mathcal{F}\{\bar{h}_{n,m}^{(k)}\}$.
- **Step 2:** $O_{n,m}^{(k)}$ is calculated by deconvolution of $i_{n,m}$ with known function $\bar{h}_{n,m}^{(k)}$ in the Fourier domain. This deconvolution method will be defined in the next paragraph.
- **Step 3:** $o_{n,m}^{(k)} = \mathcal{F}^{-1}\{O_{n,m}^{(k)}\}$.
- **Step 4:** Non-negativity constraint in the image domain is imposed by setting negative values of $o_{n,m}^{(k)}$ to zero. $\bar{o}_{n,m}^{(k)} > 0$.
- **Step 5:** $\bar{O}_{n,m}^{(k)} = \mathcal{F}\{\bar{o}_{n,m}^{(k)}\}$.
- **Step 6:** $H_{n,m}^{(k+1)}$ is calculated by deconvolution of $i_{n,m}$ with known function $\bar{o}_{n,m}^{(k)}$ in the Fourier domain. This deconvolution method will be defined in the next paragraph.
- **Step 7:** $h_{n,m}^{(k+1)} = \mathcal{F}^{-1}\{H_{n,m}^{(k+1)}\}$.
- **Step 8:** Non-negativity constraint in the image domain is imposed by setting negative values of $h_{n,m}^{(k+1)}$ to zero. $\bar{h}_{n,m}^{(k+1)} > 0$. Go back to step 1.

The deconvolution steps 2 and 6 are conducted by an inverse filter. The following inverse filter shows the filter that is used in step 2. The filter in step 6 can be found by inverting the roles of $H_{n,m}^{(k)}$ and $O_{n,m}^{(k)}$.

- if $|I_{n,m}| <$ noise level,
$$O_{n,m}^{(k+1)} = \bar{O}_{n,m}^{(k)}, \tag{3-13a}$$
- if $|\bar{H}_{n,m}^{(k)}| \geq |I_{n,m}|$,
$$O_{n,m}^{(k+1)} = (1-\beta)\bar{O}_{n,m}^{(k)} + \beta\frac{I_{n,m}}{\bar{H}_{n,m}^{(k)}}, \tag{3-13b}$$
- if $|\bar{H}_{n,m}^{(k)}| < |I_{n,m}|$,
$$\frac{1}{O_{n,m}^{(k+1)}} = \frac{(1-\beta)}{\bar{O}_{n,m}^{(k)}} + \beta\frac{\bar{H}_{n,m}^{(k)}}{I_{n,m}}, \tag{3-13c}$$

where $0 \leq \beta \leq 1$. The constant β is set initially. This inverse filter was proposed in [27] to deal with values close or equal to zero in spectra of the object or PSF.

Blind Multi-Frame Deconvolution

Other blind deconvolution methods use more than one image to reconstruct the object and PSF. Such methods are referred to as blind multi-frame deconvolution (BMFD) or blind multi-channel deconvolution. In BMFD a set of S images $\{i_{m,n|s}\}$, with S corresponding unknown PSFs $\{h_{n,m|s}\}$, are deconvolved. All images are obtained from the same object,

$$i_{n,m|s} = \sum_{k=1}^{N}\sum_{l=1}^{N} o_{k,l}h_{n-k,m-l|s} + e_{n,m}, \tag{3-14}$$

where $n, m, k, l = 1, 2, ..., N$ and $s = 1, 2, .., S$.

Different images from the same object can be obtained if the aberration is time-variant. This is often the case in *in vivo* microscopy [2]. Schulz [28] demonstrated in 1993 a practical implementation of an algorithm that uses more than one image. A year later, Yaroslavsky *et al.* [29] showed that a Wiener filter,

$$\hat{o}_{n,m} = \mathcal{F}^{-1}\left\{\frac{\sum_{s=1}^{S}(H_{n,m|s})^* I_{n,m|s}}{\sum_{s=1}^{S}|H_{n,m|s}|^2}\right\}, \tag{3-15}$$

can be used to estimate the object from more than one image. In 2017, Wilding *et al.* [3] demonstrates a fast and robust algorithm that uses iterative projections of the object and PSF into their corresponding feasible set. Those constrained sets are non-negative and normalized. Furthermore, the feasible set of PSFs is constrained by a finite support constraint. The method in [3], called tangential iterative projections (TIP), consists of four projection steps:

- **Step 1:** Object $\bar{o}_{n,m}^{(k)}$ is calculated by multi-frame linear deconvolution, Equation (3-15).
- **Step 2:** Object spectrum $O_{n,m}^{(k)}$ is obtained by applying the image domain constraints; $o_{n,m}^{(k)} = 0$ if $o_{n,m}^{(k)} < 0$ and $\sum o^{(k)} = 1$. Followed by taking the Fourier transform.
- **Step 3:** PSFs $\bar{h}_{n,m|s}^{(k+1)}$ are calculated by the modified naive inverse filter, Equation (3-6).
- **Step 4:** PSF spectra $H_{n,m|s}^{(k+1)}$ are obtained by applying the image domain constraints; $h_{n,m|s}^{(k+1)} = 0$ if $h_{n,m|s}^{(k+1)} < 0$, $h_{n,m|s}^{(k+1)} = 0$ if $(n, m) \notin \mathbb{X}$ and $\sum h_s^{(k+1)} = 1$. Followed by taking the Fourier transform.

Where $\mathbb{X}$ denotes the finite support constraint for the PSFs. Any PSF is limited by this constraint, $h_{n,m|s} \in \{h|h_{n,m} = 0, (n, m) \notin \mathbb{X}\}$. This support constraints the size on the PSFs.

A simulation of Blind Multi-Frame Deconvolution

Two experiments were conducted wherein TIP was used to deconvolve images with space invariant blur and images with space-variant blur separately. The images were made in a simulation with a phase screen. This phase screen was place outside the pupil plane at $l_1 = 0.4z_o$, see Figure 2-3. The phase screen was created by the addition of the first 40 Zernike polynomials with random coefficients between -1 and 1. The obtained phase screen was multiplied by an amplitude of 40 to reach sufficiently large aberrations. The numerical aperture, NA, during the experiment was 0.7. The images that were blurred with a space invariant PSF are formed by convolution of the object, the first sub-figure in Figure 3-2, with PSF that corresponds to the projected phase aberration onto the pupil plane with respect to the centre of the object, see Figure 2-3. The PSF for each deteriorated image is shown in the top right corner of the sub-figures in Figure 3-2. The images that were deteriorated with SV PSF are shown in Figure 3-3, again the object in shown in the first sub-figure. Every pixel is a number between 0 and 1. White Gaussian noise, with standard deviation, $\sigma = 10^{-3}$, was used during the simulations. TIP with a finite support, a circle with radius 15, was run for

Figure 3-2: The object in the first sub-figure is deteriorated by different point spread function and with the addition of white Gaussian noise with standard deviation, $\sigma = 10^{-3}$. This deterioration is performed by convolution. Convolution can be calculated efficiently in the frequency domain. The resulting images are shown in the other sub-figures. The top right corner of the blurred images shows the corresponding point spread function.

Figure 3-3: The object in the first sub-figure is deteriorated by different space-variant point spread functions and with the addition of white Gaussian noise with standard deviation, $\sigma = 10^{-3}$. Space-variant point spread functions are calculated in a simulation with a single phase screen in between the object plane and the pupil plane. Figure 2-3 shows how a phase screen models the induced phase aberration outside the pupil plane and how the aberration is projected onto the pupil plane. This allows the calculation of a point spread function that depends on the location of a point in the object. These space-variant point spread functions are used to deteriorate the object. The resulting images are shown in the other sub-figures.

Figure 3-4: The tangential iterative projections (TIP) algorithm was used to estimate the object from 5 isoplanatically deteriorated images with additional white Gaussian noise with $\sigma = 10^{-3}$. These images are shown in Figure 3-2. The finite support constraint for the point spread function was set to a radius of 15 pixels. The TIP algorithm ran for 30 iterations and a visual comparison shows that TIP succeeded in estimating the object.

Figure 3-5: The tangential iterative projections (TIP) algorithm was used to estimate the object from 5 anisoplanatically deteriorated images with additional white Gaussian noise with $\sigma = 10^{-3}$. These images are shown in Figure 3-2. The finite support constraint for the point spread function was set to a radius of 15 pixels. The TIP algorithm ran for 30 iterations and a visual comparison shows that TIP fails in estimating the object.

30 iterations. The obtained estimated object for the set of images with space invariant PSF is shown in Figure 3-4 and the estimated object for the set that was deteriorated images with SV PSF is shown in Figure 3-5. Figure 3-4 shows from visual comparison that TIP is able to estimate the object that was deteriorated by a space invariant PSF and Figure 3-5 shows that TIP cannot handle SV PSFs properly. As expected the spatial variations in the PSF cannot be corrected by a space invariant PSF.

3-1-2 Anisoplanatic Correction Methods

An anisoplanatic image formation model, as in equation (3-1), where a SV PSF is calculated for every individual pixel cannot be efficiently implemented, especially in iterative algorithms [30, 7, 31]. Computationally efficient methods are summarized in [6]. Trussel and Hunt [32] proposed a method, where the image is divided into isoplanatic subsections. This method was later used by Costello and Mikhael [18] in combination with modified Wiener filtering, Equation (3-8), in order to correct the anisoplanatic aberration. The advantage of dividing the image into isoplanatic subsections is the ability to perform efficient deconvolution via the Fourier transform. A disadvantage of such methods is the occurring of boundary artifacts [6].

Alternative models for Space-Variant Point Spread Functions

Division of an image into subsections can be performed by multiplication of the image with a mask that is one inside the subsection and zero outside. This approach leads to boundary artifacts [6]. In stead of multiplication with a mask that is constant inside a subsection, the weights of those masks can be chosen differently. Nagy and O'leary [5] use a bi-linear interpolation mask for the image. Hirsch *et al.* [7] apply the bi-linear mask to interpolate a limited number of PSFs to model a SV PSF. Flicker and Rigaut [8] perform decomposition of PSF modes. Denis *et al.* [6] calculate optimal local weights for the mask and locally optimal PSFs.

Image Interpolation

The method in [5] uses bi-linear interpolation masks to interpolate the local results. The object is convolved with a local space invariant PSF. Thereafter, the local results are interpolated via multiplication with interpolation masks. Figure 3-6 summarizes this method. The masks weights are chosen to performs bi-linear interpolation, therefore the mask is positive and the positivity constraint on the PSF is conserved.

Point Spread Function interpolation

Another approach is to first apply the interpolation mask on the object and then perform convolution with space invariant PSF. Denis *et al.* [6] shows that this approach is similar to the model in [7]. Denis *et al.* conclude that this method preserves positivity and normalization of the PSF. Figure 3-7 shows a schematic representation of this method. According to Denis *et al.* [6] this method is the most natural model. More importantly, according to their experiments and between the methods they considered, PSF interpolation as in [7, 31] is

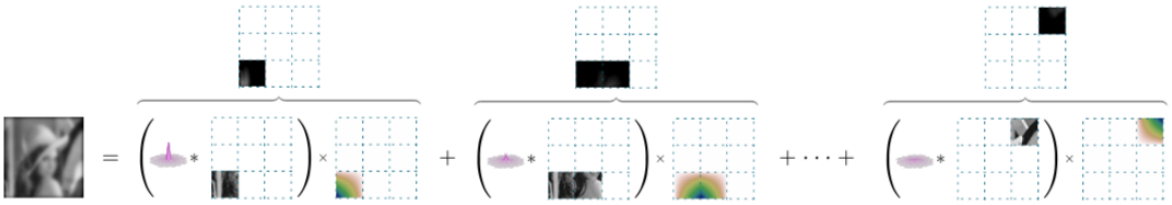

Figure 3-6: The approach of Nagy and O'Leary [5] approximates the space-variant point spread function by interpolating the images that are a result of convolution of the object and the local space invariant point spread function. Bi-linear interpolation is performed by multiplication with a mask that has the correct interpolation weight. (Source: [6])

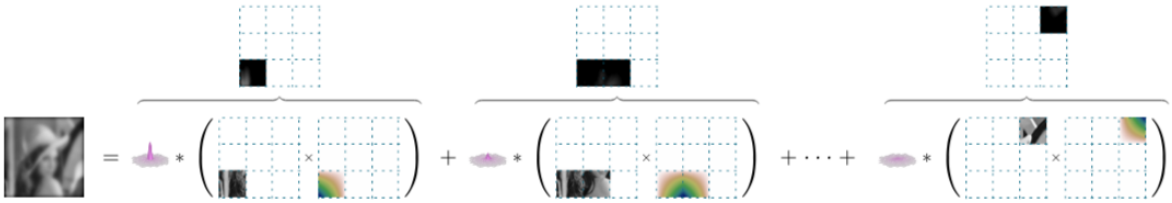

Figure 3-7: The approach of Hirsch *et al.* [7] approximates the space-variant point spread function by multiplication with bi-linear interpolation masks. First the object is multiplied by a mask that performs bi-linear interpolation of the point spread functions. Then the result is convolved with a local space invariant point spread function. (Source: [6])

the second best approximation model, after their optimal local approximation method. The advantage of this method over the optimal local approximation method is that only four interpolation masks have to be created. These predetermined interpolation masks have to be calculated only once. This is a huge advantage in terms of computational load, especially when this method is applied in an iterative loop to perform blind multi-frame deconvolution.

Optimal Local Approximation

Denis *et al.* [6] proposed a method similar to the method in [7]. In [7] bi-linear interpolation masks are used to interpolate the PSFs in order to approximate the SV PSF. In [6] the local PSFs and interpolation weights are chosen to minimize the approximation error. This method can be represented by the schematic drawing in figure Figure 3-8.

Point Spread Function Decomposition Methods

Besides the methods that use a locally nonzero mask to handle with subsection individually, there is a group of methods that uses a limited number of space invariant PSFs and global masks that weights the influence of the space invariant PSFs to model the SV PSF. Figure 3-9 shows a schematic representation for the group of methods that use global masks and a set of space invariant PSFs to approximate the SV PSF. Flicker and Rigaut [8] approximate the SV PSF by decomposition into space invariant modes. before convolution the image is weighed for every space invariant PSF by a global mask. Miraut and Portilla [9] and later Sroubek *et al.* [10] decompose the the SV PSF into space invariant modes by means of the

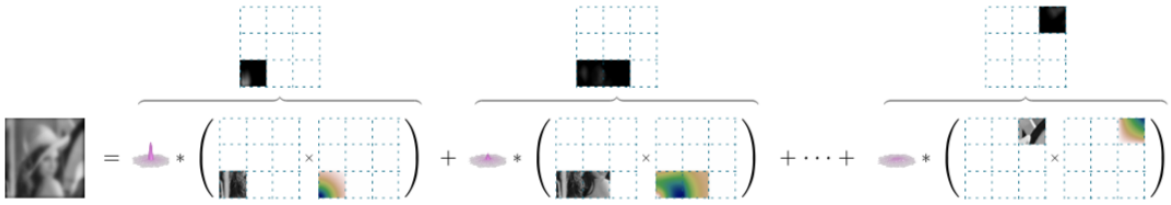

Figure 3-8: The approach of Denis *et al.* [7] approximates the space-variant point spread function by multiplication with optimal interpolation masks. First the object is multiplied by a mask that performs bi-linear interpolation of the point spread functions. Then the result is convolved with a local optimal space invariant point spread function. (Source: [6])

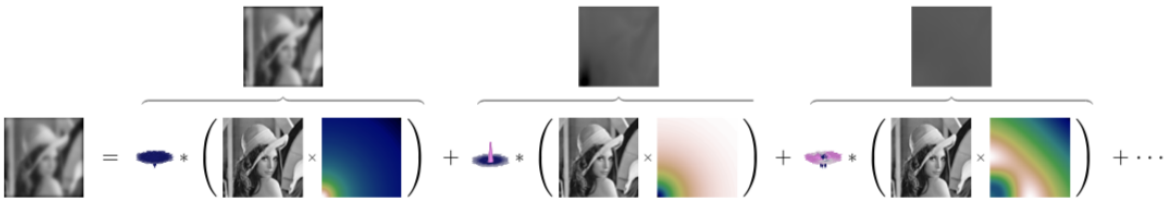

Figure 3-9: The methods used in [8, 9, 10] use a limited number of space invariant point spread functions and a set of global masks to weight the image according to the influence of each space invariant point spread function. These decomposition methods are approximating the space-variant point spread function. (Source: [6])

singular value decomposition. An advantage of decomposition of the SV PSF by the singular value decomposition is that it is globally optimal with respect the the approximation error [6]. On the other hand, according to Denis *et al.* [6], the use of global methods comes with large computational load.

Blind Anisoplanatic Correction

In order to correct a deteriorated image without knowing the aberration of SV PSF, blind correction methods are required. An anisoplanatic correction method that is blind, estimates both the object and the aberration or SV PSF. Most blind anisoplanatic correction methods [32, 33, 34] use the assumption that the image can be divided into isoplanatic subsections. For every subsection the corresponding object is estimated by conventional blind isoplanatic deconvolution.

Hirsch *et al.* [7] demonstrates a framework to perform blind anisoplanatic correction. In their framework they assume an image formation model as presented in Figure 3-7. First the object is divided in subsections by multiplication with local nonzero masks. These masks are chosen to perform interpolation of the local PSFs. The condition for these masks, is that they add up to 1. This property is always satisfied after normalization. After multiplication with a mask, the weighted object is convolved with a local space invariant PSF. All subsections are added to form the image. The object and local space invariant PSFs are estimated alternately. In the experiment conducted by Hirsch *et al.*, they used 100 images to perform the correction. First the local space invariant PSFs are estimated by parameterizing the PSF and using constrained optimization. Then the estimated object is updated by deconvolution with a local space invariant point spread function. These two steps form an iterative loop. In every

iteration a new image is used to calculate the corresponding local PSFs and to update the estimated object.

Chapter 4

A New Computational Approach to Correct Space-Variant Phase Aberrations

The methods and theory known in literature regarding to the correction of deteriorated images motivated the development of a new algorithm. The work of Denis *et al.* [6] suggests the use of a computational efficient image formation model where local deconvolution can be applied. Wilding *et al.* [3] demonstrated blind multi-frame deconvolution by means of tangential iterative projections (TIP). This first part of this chapter provides a motivation for the use of both methods in one algorithm in order to correct for anisoplanatic aberrations in microscopic images. The second part demonstrates the use and limitation of the algorithm. Further improvements to the algorithm are discussed in Chapter 6.

4-1 Efficient Restoration by Local Deconvolution

A general approach to model image formation is given by Equation (3-1), where is assumed that a point on the object, $o_{k,l}$, will spread out in the image by a space-variant (SV) point spread function (PSF), $\tilde{h}_{n,m,k,l}$. Without any assumptions on the SV PSF a correction method must be developed to correct for all pixels in the image individually. As suggested by Trussel and Hunt [32] and Nagy and O'leary [5], image formation can be modelled in a computational efficient way. It is assumed that images are locally the result of convolution. This assumption is supported by Equation (2-12). Assuming that the SV PSF is changing continuously and assuming small changes in the PSF on an ϵ-neighbourhood, image formation is locally the result of convolution of the object with a local space invariant PSF and the addition of noise.

$$i_{k,l} = o_{k,l} * h_{k,l} + e_{k,l}, \quad i_{k,l} \in V_\epsilon \tag{4-1}$$

where V_ϵ is the ϵ-neighbourhood around a point p, where $h_{k,l}$ is the exact local PSF. Assuming the imaging model Equation (3-1), Equation (4-1) is true for any ϵ, since all errors are

contained in $e_{k,l}$.

$$e_{k,l} = i^*_{k,l} - i_{k,l} = i^*_{k,l} - o_{k,l} * h_{k,l}, \tag{4-2}$$

where $i^*_{k,l}$ is the true image. Considering continuous changes in the PSF it follows that the error becomes smaller for smaller values for ϵ.

4-1-1 Local Deconvolution by Tangential Iterative Projections

As convolution between an object and PSF can be used to describe the formation of an image locally, local deconvolution can be used to correct for anisoplanatic aberrations in the image. In blind anisoplanatic deconvolution the SV PSF is unknown. Therefore, the size of the error is unknown. For this reason a robust blind deconvolution algorithm is applied to perform this local blind deconvolution. TIP is a robust algorithm to perform blind multi-frame deconvolution. Another advantage of TIP is the use of multiple images. Wilding *et al.* [3] describe that more images should be used, because some frequency content in the object might not be captured by the camera in a single image.

Interpolation of Local Results

A known disadvantage of local deconvolution is the formation of edge artifacts near the edges of the corrected region in the image. This effect is demonstrated in [6]. The work of Denis *et al.* [6], Hirsch *et al.* [7] and Nagy and O'leary [5] motivate the use of interpolation. In their works, interpolation is used to model image formation by local convolution between object and PSF. Here bi-linear interpolation masks will be applied to combine local deconvolution results in order to reduce edge artifacts.

4-1-2 Tangential Iterative Projections Algorithm for Anisoplanatic Aberrations

The new method to correct for anisoplanatic aberrations in microscopic images requires multiple images of the same object. These images will be divided in overlapping subsections such that interpolation can be applied after deconvolution. Let $\mathcal{I}_\mathcal{S}$ be the set containing S images, $\{i_1, i_2, \cdots, i_S\}$, and let $i_{p,q|s}$ denote subsection p, q of image i_s. Figure 4-1 shows an image that is divided in subsections. The subsection $i_{p,q}$ is shaded in red. Every subsection in Figure 4-1 has four quadrants. Subsections $i_{p,q}$ and $i_{p,q+1}$ have two overlapping quadrants. On every subsection, image formation by local convolution of the object and local PSF is assumed. The local PSF for subsection $i_{p,q}$ in image s is denoted by $h_{p,q|s}$.

Similar to the TIP algorithm, tangential iterative projections algorithm for anisoplanatic aberrations (TIP3A) has 4 main steps, or projections. In the first step the object is estimated by multi-frame linear deconvolution. In TIP3A, multi-frame linear deconvolution is used to estimate the object within all subsections, thereafter bi-linear interpolation is used to combine all local results. The second step projects the object on the feasible set of all possible objects. In the third step all local PSFs are estimated by single-frame linear deconvolution. Isolation of the corresponding subsection in this step is performed by multiplication with an apodization kernel. The fourth and last step is the projection of the estimated local PSF on the feasible set of all possible PSFs.

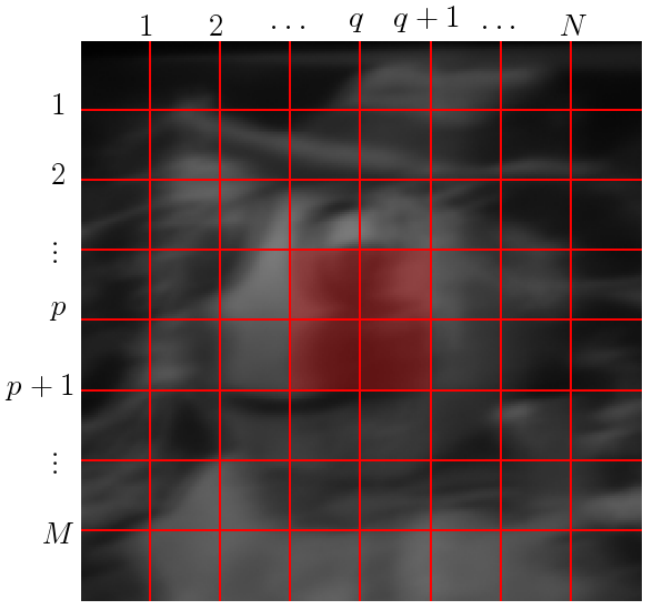

Figure 4-1: The deteriorated image is divided in M by N overlapping subsections. subsection $i_{p,q}$ is highlighted in red. Every subsection has four quadrants. The next subsection to the right, $i_{p,q+1}$, has two overlapping quadrants with subsection $i_{p,q}$.

Object Step in Fourier Domain

The algorithm is initialized by assuming that all local PSFs are delta functions, $h_{p,q|s} = \delta[m,n]$. As a result, the first estimated object is pixel-wise average of all images. During the kth iteration, multi-frame linear deconvolution is used to estimate the object subsection

$$\bar{o}_{p,q}^{(k)} = \mathcal{F}^{-1}\left\{\frac{\sum_{s=1}^{S}\left(H_{p,q|s}^{(k)}\right)^{*} I_s}{\sum_{s=1}^{S}|H_{p,q|s}^{(k)}|^2}\right\}, \tag{4-3}$$

where capital letters are used to denote the two dimensional Fourier transform and H^* is the complex conjugate of H. As the subsections are overlapping, weights are applied to every object subsection. Every object subsection is multiplied element-wise by a weight or mask, $W_{p,q}$. The weights are chosen such that $\sum_{p=1}^{M}\sum_{q=1}^{N} W_{p,q}$ is one for every pixel. Here, the weights are congruent to a bi-linear interpolation mask, as in [7]. Figure 4-2 shows the weight of a bi-linear interpolation mask. After multiplication of the object subsection with the corresponding weight, the weighted object subsection is formed, Figure 4-3. Summation of these weighted object subsection creates the estimated object

$$\bar{o}^{(k)} = \sum_{p=1}^{M}\sum_{q=1}^{N} \bar{o}_{p,q}^{(k)} W_{p,q}. \tag{4-4}$$

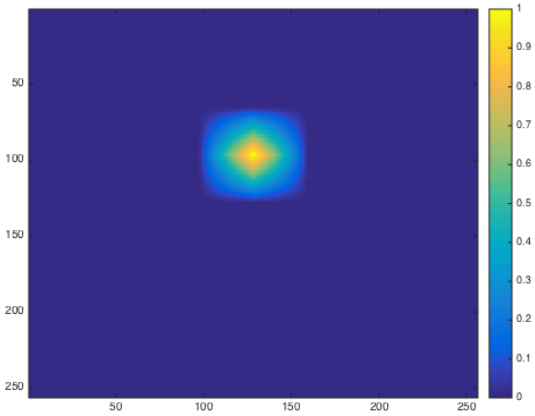

Figure 4-2: The bi-linear interpolation masks is used to create one object from all overlapping subsections. Every subsection is multiplied with a corresponding mask. The sum of these masks is one uniformly. The weight of these masks represents the contribution to a point as in bi-linear interpolation.

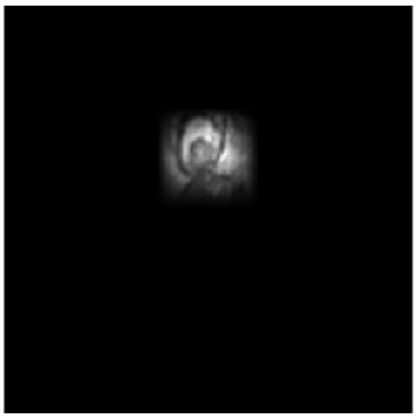

Figure 4-3: The weighted object subsection is the object multiplied with the interpolation mask, Figure 4-2. The estimated object is the sum of all weighted object subsections.

Object Step in Spatial Domain

This step is similar to the second projection step in TIP. The object is project on the feasible set of all possible object. This is done by applying the following object constraints. The intensity of the estimated object must be positive

$$o^{(k)} = 0, \quad \text{if} \quad \bar{o}^{(k)} < 0 \tag{4-5}$$

and the object is normalized

$$\sum o^{(k)} = 1. \tag{4-6}$$

The object spectrum is given by the Fourier transform of the object

$$O^{(k)} = \mathcal{F}\left\{o^{(k)}\right\}. \tag{4-7}$$

PSF Step in Fourier Domain

The local PSF can be estimated by local single-frame linear deconvolution. The object can be deconvolved with the image locally by isolating the correct part in the object. A Gaussian apodization kernel is used to isolate the corresponding part of the object. Apodization also reduces edge effects, such as ringing and ghosts [12]. Apodization around point $p_{i,j}$ is performed by multiplying the object with kernel

$$K[m,n] = e^{-\frac{(m-i)^2+(n-j)^2}{w}}, \tag{4-8}$$

where w is the width parameter of the Gaussian apodization kernel. Let $K_{p,q}$ denote the apodization kernel corresponding to object subsection, $o_{p,q}$, and local PSF, $h_{p,q|s}$. Then the estimated local PSF is give by linear single-frame deconvolution of the apodized object and image.

$$\bar{h}_{p,q|s}^{(k+1)} = \mathcal{F}^{-1}\left\{\frac{I_s}{O_{K_{p,q}}^{(k)}(|O_{K_{p,q}}^{(k)}| < \epsilon) = \infty}\right\}, \tag{4-9}$$

where $O_{K_{p,q}}^{(k)} = \mathcal{F}\{o^{(k)}K_{p,q}\}$.

PSF Step in the Spatial Domain

The final step ensures that the properties of a PSF are satisfied. The estimated PSF, $\bar{h}_{p,q|s}^{(k+1)}$, is projected on the feasible set of possible PSFs. Similar to TIP, Let $\mathbb{X}$ denote the limited support constraint for the PSFs. The set of all possible PSFs, $\mathcal{H} = \{h|h_{p,q|s}[i,j] = 0, [i,h] \notin \mathbb{X}\}$, is limited to the size of the support constraint. Furthermore, the PSF is an intensity distribution that contains only non-negative real values and is normalized.

$$h_{p,q|s}^{(k+1)} = 0, \quad \text{if} \quad \bar{h}_{p,q|s}^{(k+1)} < 0 \tag{4-10}$$

and

$$\sum h_{p,q|s}^{(k+1)} = 1. \tag{4-11}$$

As a result any PSF, h, can be written as the sum of two components. The tangential component of h, denoted as $h_{\|}$, is contained in $\mathcal{H}$. The normal component $h_{\perp}$ are the pixels of the PSF that are not contained in $\mathcal{H}$.

$$h = h_{\|} + h_{\perp}, \quad h_{\|} \in \mathcal{H},\ h_{\perp} = 0. \tag{4-12}$$

Finally, the PSF sectrum is given by the Fourier transform of the estimated PSF

$$H_{p,q|s}^{(k+1)} = \mathcal{F}\left\{h_{p,q|s}^{(k+1)}\right\}. \tag{4-13}$$

In TIP3A, these four steps are repeated consecutively.

4-2 Experiments with TIP3A

TIP3A is an algorithm that can handle spatial and temporal variations in the PSF. Since local deconvolution of aberrated images is used, it can be expected that the total number of subsection has an influence on the image quality of the estimated object. Furthermore, the algorithm parameters such as the threshold of division, ϵ, the apodization width, w, the radius of the limited support constraint, $r_{\mathbb{X}}$, and the number of iterations can influence in the quality of the estimated object. Besides the algorithm parameters, external parameters such as variations in the PSF and noise are affecting the outcome of the algorithm. The purpose of the section is to tune the algorithm parameters and demonstrate some limitations of the algorithms. Chapter 5 will elaborate different image quality metrics such that quantitative results and empirical convergence can be shown. Further fine-tuning of the algorithm can be done after an adequate image quality metric is selected.

4-2-1 Obtaining Test Images From Simulations

Simulations with a single phase screen were performed to obtain sets of images with anisoplanatic aberrations. The projection method as shown in Figure 2-3 was used to calculate the SV phase aberration. This method allows the calculation of every individual PSF for every point in the object.

Defining the System Geometry

The imaging system geometry is demonstrated in Figure 2-3. A phase plane is placed at distance l_1 to the right of the object plane. The pupil plane is at distance l_2 tot he right of the phase plane. Therefore, the object distance $z_o = l_1 + l_2$. A thin lens is with numerical aperture, NA, is located in the pupil.

Creating the Phase Screen

A phase screen, ϕ, is placed in the phase plane. This phase screen is the sum of N_Z Zernike polynomials with maximum amplitude A_Z

$$\phi = A_Z \sum_{N=1}^{N_Z} a_N Z_N, \tag{4-14}$$

where $-1 < a_N < 1$ is a random number.

Creating an Image

The object in Figure 4-4 was placed in the object plane. The PSF for every pixel can be calculated by the projection method in Figure 2-3. By geometry, the optical path from a point in the object to the pupil has an intersection plane in the phase plane. This intersection plane is unique for that point in the object. The phase aberration in the intersection plane is scaled in the x and y direction to fit exactly inside the pupil. As a result Equation (2-12) can be used to calculate the PSF. Equation (2-14) can be used to form the noiseless image with anisoplanatic aberrations.

The Addition of Noise

Noiseless sets of images were saved such that noise with different amplitudes could be added to the images later. In the noiseless images every pixel is a value between 0 and 1. White Gaussian noise with a standard deviation, σ, was later added to the images.

4-2-2 Comparison with Varying Number of Subsections

In this section 256 by 256 images are used. The imaging system's geometry is given by $l_1 = 2$, $l_2 = 3$, $NA = 0.7$. The Phase screens are given by $A_Z = 40$ and $N_Z = 40$. The set consists

Figure 4-4: Ground truth or scientific object.

of 10 images for 10 random realizations of the phase screens. The set of anisoplanatic images is shown in Appendix A. Besides the set of images with anisoplanatic aberrations, there is a set of images with isoplanatic aberrations. This set of formed by convolution of the object and the central local PSF of the anisoplanatic images. The performance of the TIP3A is compared visually to the performance of TIP. This is done by comparing visual details in the images. The noise in the images is white Gaussian noise with standard deviation $\sigma = 10^{-5}$.

The ground truth or scientific object used during the simulations is given in Figure 4-4.

Algorithm Comparison with Isoplanatic Aberrations

The TIP algorithm is designed to correct isoplanatic aberrations. TIP3A with 1 subsection and a large apodization width is equivalent to the TIP algorithm. In order to show the relation between TIP and TIP3A, the TIP algorithm is compared to TIP3A with apodization width, $w = 2000$, limited support radius, $r_{\mathbb{X}} = 6$, threshold, $\epsilon = 10^{-4.4}$, and varying number of subsections. These algorithm parameters were found by tuning the algorithm first. Variation should only be possible due to variations in the local frequency content of the images. If an image is locally flat, then after apodization the input signal is not persistently exciting for identification of the local PSF. Therefore, only for sufficiently large apodization it is hypothesized that for isoplanatically deteriorated images TIP and TIP3A will produce similar results regardless of the number of subsections in TIP3A.

An experiment was conducted where 10 images with isoplanatic aberrations were the input for the TIP algorithms and for TIP3A with M by N subsections. This algorithm was repeated for $M = N$ equal to $1, 3, 7$ and 15. This corresponds to a total number of $1, 9, 49$ and 225

subsections respectively. The estimated object after $1, 5, 10, 15, 20$ and 25 iterations of the algorithm are depicted in Appendix B.

Visual comparison of the Figures B-1 - B-5 in Appendix B show that input images with isoplanatic aberrations will lead to similar output for TIP and TIP3A.

Algorithm Comparison with Anisoplanatic Aberrations

TIP3A differentiates from TIP when the input images contain anisoplanatic aberrations. If anisoplanatic aberrations occur, the PSF is space variant. If the PSF is space variant, it is favorable to use a small apodization, such that a constant local PSF can be assumed. On the other hand, if the apodization is too small, the input signal might not be persistently exciting for PSF identification. Apodization and location influence the persistence of excitation of the input signal. Therefore, the maximum performance of the algorithm is always a trade-off between the number of subsection, M, N, apodization width, w, and limited support radius $r_{\mathbb{X}}$.

A similar experiment was conducted with 10 images that were deteriorated with anisoplanatic aberrations. The images were used as input for TIP and TIP3A with $1, 9, 49$ and 225 subsections. The results are presented in Appendix B.

Visual comparison of the Figures B-6 - B-10 in Appendix B show that the performance of the TIP3A algorithm is clearly dependent on the number of subsections. Close inspections of visual details, such as the edge of the hat, the straw hair, the plant in the background or the puppet's collar, show that the restoration quality becomes higher as the number of subsection increases from 1 to 9 to 49. However, the restoration quality of the estimated object is lower for 225 subsections than for 49 subsections.

4-2-3 Limitations of the Algorithm

Large variations in the SV PSF form a limitation of this computationally efficient algorithm. If the variations in the SV PSF increase, the error in Equation (4-2) becomes larger. Consequently, the image quality of the estimated object goes down. TIP3A is an algorithm that can handle anisoplanatic aberrations, but it relies on isoplanatic regions throughout the images. An other limitation of the algorithm is formed by the limited support constraint. This constraint is necessary for the convergence of the algorithm. However, if the limited support radius is chosen too small, the estimated PSF will be smaller than the true PSF. If the estimated PSF is too small, deconvolution is performed with only a part of the true PSF. This will leave fragments in the estimated object that were visible in the deteriorated images. These residuals are unwanted.

In this chapter is shown that TIP3A can handle anisoplanatic aberrations or SV PSFs. TIP3A is used in Chapter 5 to compare different image quality metrics. The image quality of the estimated object can be measured by different metric. In Chapter 5 a metric is selected that will be used throughout the thesis. In Chapter 6, an algorithm will be designed that overcomes the limitations of TIP3A. The chosen metric will be used to show that this improved algorithm performs better than TIP3A.

Chapter 5

Measuring the Image Quality of the Estimated Object

A new computational method that can reconstruct images with anisoplanatic phase aberrations is demonstrated in Chapter 4. From visual inspection can be concluded that the tangential iterative projections algorithm for anisoplanatic aberrations (TIP3A) algorithm can handle anisoplanatic aberrations, while tangential iterative projections (TIP) [3] can only correct for isoplanatic aberrations. The performance of TIP3A can be compared to other algorithms if an adequate quality measure is used. In this chapter, different quality metrics will be compared. The aim of this chapter is to select a metric that can be used to compare the performance of image reconstruction algorithms.

5-1 Method

The selection of an adequate measurement for image quality is done in three main steps. The first step is a discussion of metrics commonly used in imaging. Thereafter, in the second step experiments are conducted. In these experiments TIP3A is used and the convergence of the algorithm is measured with different metrics. In the last step, the convergence curves will be compared to the visual results. This will lead to a conclusion, what metric represents the image quality of the estimated object the best.

5-1-1 Image Quality Measurements

Image quality in this section is the resemblance between the estimated object and the ground truth. It is important to note that the original image is used as a reference image. Let o denote the true scientific object and $\hat{o}$ denote the estimated object.

Mean Squared Error

The mean squared error (MSE) is used as an error metric in all types of engineering and research. The sum of squared errors or the mean of squared errors form also the building block for many other error metrics [35].

$$MSE = ||o - \hat{o}||_F^2 / n^2, \tag{5-1}$$

where n^2 is the number of pixels for an n by n image. Note that the Frobenius norm squared, $||o - \hat{o}||_F^2$, of an image is the sum over all squared errors.

Peak Signal-to-Noise Ratio

The peak signal-to-noise ratio (PSNR) is used as a comparison metric between the ground truth and the estimated object in the original publication of TIP [3]. PSNR is the ratio between the maximum intensity and the MSE on a logarithmic scale. The PSNR is therefore measured in decibels (dB).

$$PSNR = 10 \log_{10} \left(\frac{\max\{o\}^2}{MSE} \right) \tag{5-2}$$

Therefore, the PSNR for an object with maximum intensity, $\max\{o\} = 1$, is given by

$$PSNR = -10 \log_{10} \left(||o - \hat{o}||_F^2 / n^2 \right). \tag{5-3}$$

Normalized Root Mean Square Error

Close related to the MSE is the normalized mean squared error (NMSE). This metric is specifically designed for the comparison of image-reconstruction algorithms [35].

$$NMSE = \frac{||o - \hat{o}||_F^2}{||o||_F^2} \tag{5-4}$$

Fourier Ring Correlation

Fourier ring correlation (FRC) measures the normalized cross-correlation between the scientific object and the estimated object on a ring in the Fourier domain. FRC is originally a method to determine the resolution reconstructed images in electron microscopy [36] (cited in [37]). In this thesis FRC will be used to to measure the similarity between the original object and the estimated object at a specific set of spatial frequencies.

$$FRC = \frac{\sum_{r_i \in r} O[r_i] \cdot \hat{O}^*[r_i]}{\sqrt{\sum_{r_i \in r} |O[r_i]|^2 \cdot \sum_{r_i \in r} \left| \hat{O}[r_i] \right|^2}}, \tag{5-5}$$

where capital letters are used to denote the Fourier transform and O^* is the complex conjugate of O.

Structural Similarity

Structural similarity (SSIM) is a metric inspired be the human visual system [38]. SSIM is a method designed to measure the visual similarity of two images.

$$SSIM = \frac{(2\mu_o\mu_{\hat{o}} + c_1)(2\sigma_{o\hat{o}} + c_2)}{(\mu_o^2 + \mu_{\hat{o}}^2 + c_1)(\sigma_o^2 + \sigma_{\hat{o}}^2 + c_2)}, \tag{5-6}$$

where μ_o, $\mu_{\hat{o}}$, σ_o, $\sigma_{\hat{o}}$ and $\sigma_{o\hat{o}}$ are the local means, standard deviations and cross-covariance for the object and estimated object respectively. c_1 and c_2 are constants.

Conclusion

MSE and PSNR and often used for the evaluation of the performance of image reconstruction algorithms. The NMSE is considered an improvement of the MSE. Since the MSE, PSNR and NMSE are all three based on the Frobenius norm of the error between the original object and the estimated object, only one metric will be considered. As PSNR was used to measure the performance of TIP, it will be considered here. PSNR, FRC and SSIM will be used as error metrics in the experiments.

5-1-2 Comparing Measurements

The estimated object will be compared to the ground truth or scientific object. In [3] is demonstrated that TIP is empirically convergent if the input image has only isoplanatic phase aberrations. In Section 4-2 is shown that TIP does not converge necessarily when the images have anisoplanatic aberrations. From the figures in Appendix B can also be concluded visually, that the final image quality is better if the input images were deteriorated isoplanatically.

The experiment in Section 4-2 was repeated for TIP with isoplanatic input images, TIP with anisoplanatic input images and TIP3A with anisoplanatic input images. The images with anisoplanatic aberration that were used in this experiment are shown in Appendix A. The images with isoplanatic aberrations are made by convolution of the scientific object and the central local PSF of the anisoplanatic images. The algorithm parameters that were used are: $r_{\mathbb{X}} = 6$, $\epsilon = 10^{-4.4}$ for both TIP and TIP3A and $w = 2000$, $M = N = 7$ for TIP3A. The image quality is measured with PSNR, FRC and SSIM. The visual results are depicted in Figures B-1, B-6 and B-9 in Appendix B.

The results for TIP with input images that were deteriorated with isoplanatic phase aberrations will be used as a reference measurement for the image quality of the estimated object. Since empirical convergence was shown for TIP for images with isoplanatic aberrations, this reference line gives an empirical optimum. As the input in the reference case has only isoplanatic aberrations, the image quality of the reference case must be the best. If images with anisoplanatic phase aberrations were used as input for the TIP algorithm, it can be seen in Figure B-6 that the image quality is low. In Figure B-9 can be seen that TIP3A can handle the isoplanatic phase aberrations. The image quality of estimated object for TIP3A is better compared to TIP. An adequate image quality metric can represent these visual properties.

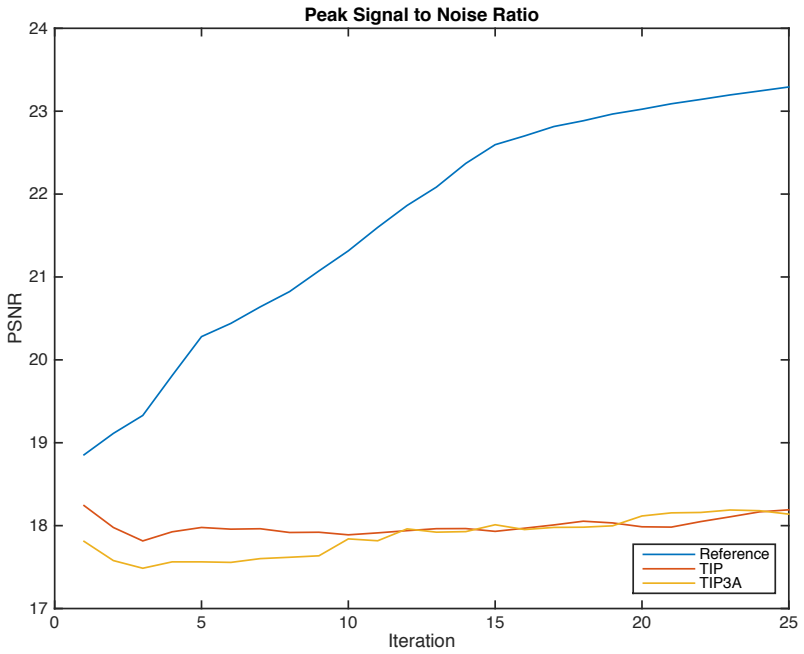

Figure 5-1: The image quality of the estimated object over 25 iteration, measured with PSNR. The reference case is the result after feeding 10 images with isoplanatic aberrations in the TIP algorithm. Since the input is isoplanatic, it must hold the best result. In this figure TIP and TIP3A for 10 images with anisoplanatic phase aberrations are compared to the reference case.

Results

The image quality during the experiment was measured with PSNR, FRC and SSIM. Quantitative results are shown in Figures 5-1, 5-2 and 5-3.

5-2 Conclusion

Figure 5-1 shows that the image quality in TIP and TIP3A is similar, this does not correspond to the visual results. Therefore, PSNR does not represent the image quality adequately. Both FRC and SSIM represent the visual properties that were discussed. The reference measurement shows the best image quality and after some iterations the image quality of the estimated object is better in TIP3A than in TIP.

In Figure 5-2 can be seen that the reference case has the highest FRC for all iterations. More importantly, it shows that TIP3A has a better image quality for the estimated object compared to TIP.

Figure 5-3 shows the same characteristics for SSIM. It shows that the reference case has the best results and that TIP3A performs better in handling anisoplanatic aberrations than TIP.

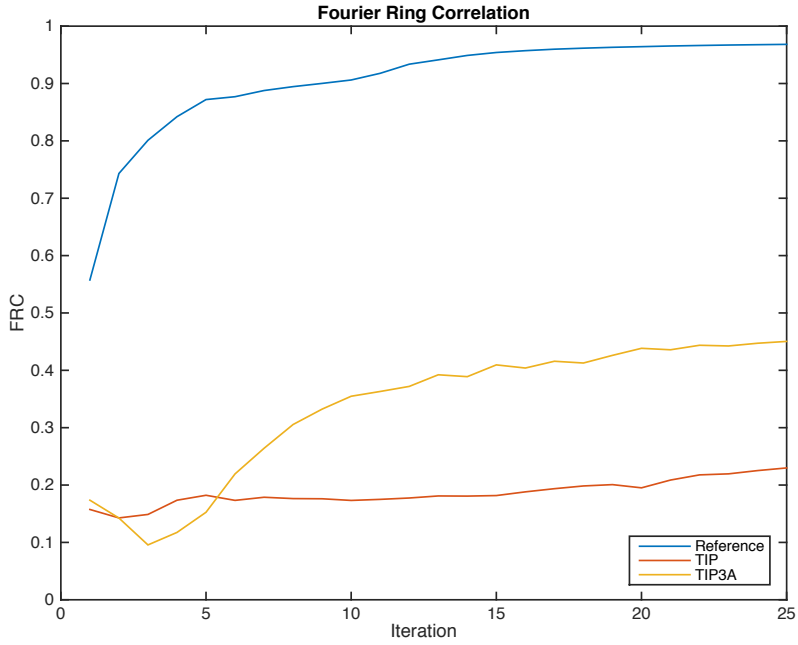

Figure 5-2: The image quality of the estimated object over 25 iteration, measured with FRC. The reference case is the result after feeding 10 images with isoplanatic aberrations in the TIP algorithm. Since the input is isoplanatic, it must hold the best result. In this figure TIP and TIP3A for 10 images with anisoplanatic phase aberrations are compared to the reference case.

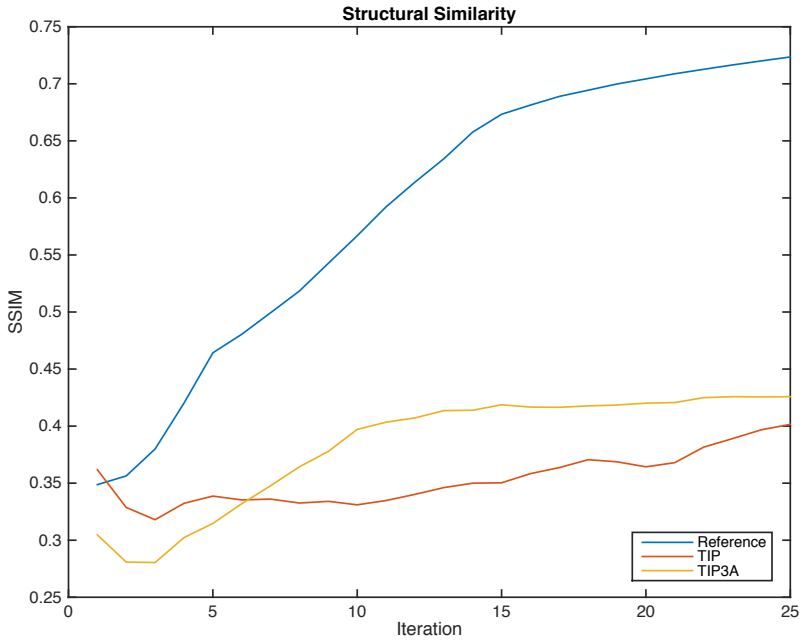

Figure 5-3: The image quality of the estimated object over 25 iteration, measured with SSIM. The reference case is the result after feeding 10 images with isoplanatic aberrations in the TIP algorithm. Since the input is isoplanatic, it must hold the best result. In this figure TIP and TIP3A for 10 images with anisoplanatic phase aberrations are compared to the reference case.

discussion

Both FRC and SSIM were able to show that TIP3A performs better in handling anisoplanatic aberrations than TIP. It was not shown how TIP3A and TIP handle noise. If the same experiments were conducted with the addition of noise, FRC would have shown a similar graph to Figure 5-2. SSIM is more sensitive to noise than FRC. For this reason, FRC will be used in this thesis as a metric for image quality of the estimated object. In order to measure the influence of noise, both FRC and SSIM will be used.

Chapter 6

An Improved Computational Approach to Correct Space-Variant Phase Aberrations

In Chapter 4 tangential iterative projections algorithm for anisoplanatic aberrations (TIP3A) was presented as a methodology for retrieving the unknown scientific object. Some quantitative results are shown in Chapter 5. The aim of this chapter is to improve the method presented in Chapter 4. This is done by testing the proposed improvements in experiments.

6-1 Spatial Domain Constraints

two steps in TIP3A are the object and point spread function (PSF) step in the spatial domain. In this section, changes to the steps in the spatial domain and considered. In experiments is shown if the proposed changes results in increased image quality of the estimated object.

6-1-1 Object Step in the Spatial Domain

In TIP3A the estimated object must satisfy some object constraints. One of these *a priori* is non-negativity of the object's intensity measurement. The estimated object is given by discrete intensity measurements. It is known that the intensity is non-negative. In TIP3A, the object is formed by summation of all weighted object subsections, Equation (4-4).

In TIP3A, the object constraints are applied after the object is formed. It can be considered to apply the non-negativity constraint to the object subsections first. Both methods are compared in an experiment. TIP3A was used with $r_{\mathbb{X}} = 6$, $\epsilon = 10^{-4.4}$, $w = 2000$ and $M = N = 7$. Thereafter the same simulation was performed, however the non-negativity constraint was applied on the object subsections in stead of on the estimated object. The experiment was conducted with the images in Appendix A with white Gaussian noise having a

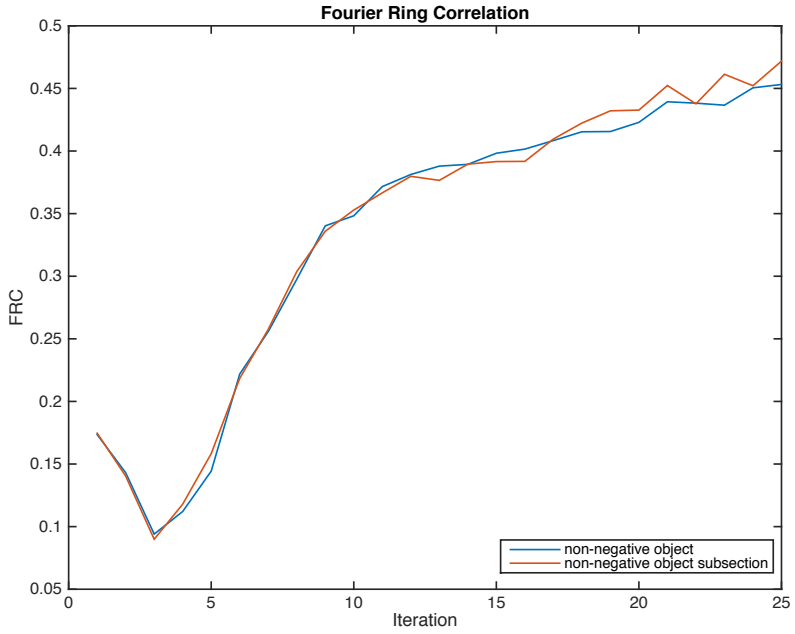

Figure 6-1: The image quality of the estimated object over 25 iterations, measured with FRC. In this figure can be seen that applying the non-negativity constraint on either the estimated object or estimated object subsection, does not make difference in image quality.

standard deviation $\sigma = 10^{-5}$. The same experiment was repeated under high noise conditions, $\sigma = 10^{-2}$. Both experiments shows the same results. The result for the first experiment is shown in Figure 6-1. In Figure 6-1 can be seen that the image quality for all iterations is almost similar. Applying the non-negativity constraint on the object in the spatial domain results in a similar image quality of the estimated object compared to applying this constraint on the estimated object subsection.

6-1-2 PSF Step in the Spatial Domain

The limited support constraint is important for the convergence of TIP [3] and TIP3A. When anisoplanatic aberrations play a role, the PSF is space-variant (SV). Therefore, it is proposed to use a SV limited support region called adaptive limited support. A SV limited support region is a circular region where the location of the centre is dependent on the estimated local PSF. Two suggestions are considered to make this support region adaptive. The first is adaptation of the centre of the limited support region to the centre of gravity of the estimated PSF. In the second method, the point of maximum intensity is used as centre for the limited support region. Both methods are aimed at translating the centre of the limited support region, such that most of the local PSF is inside the limited support region.

Adaptation to Centre of Gravity of the Intensity Distribution

In an experiment, two simulations are conducted. TIP3A was used with $r_{\mathbb{X}} = 6$, $\epsilon = 10^{-4.4}$, $w = 2000$ and $M = N = 7$. In the first simulation TIP3A was used without any modifications.

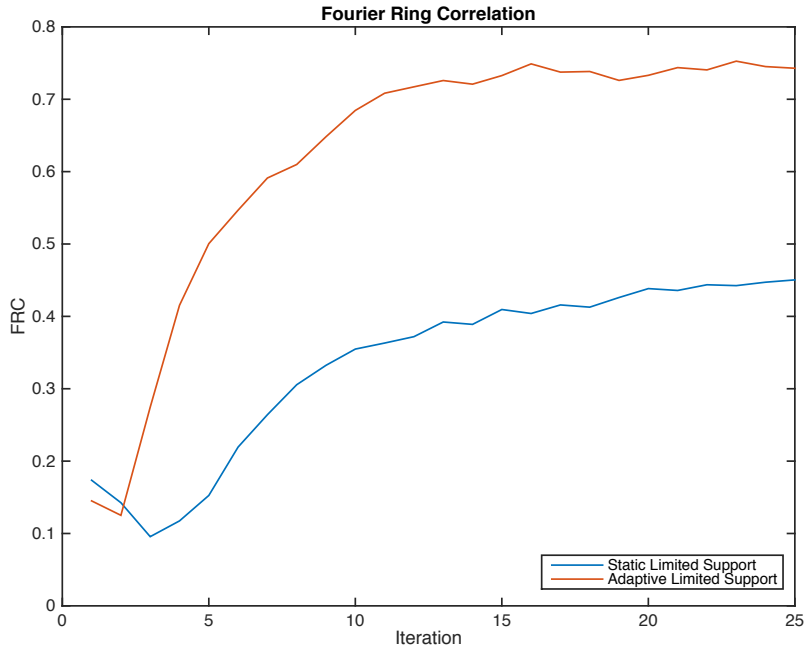

Figure 6-2: The image quality of the estimated object over 25 iterations, measured with FRC. In this figure can be seen that adaptive limited support with the centre of the limited support region set to the centre of gravity of the estimated PSF, increases the image quality of the estimated object.

Adaptive limited support was used during the second simulation. The centre of the limited support region was set to be the centre of gravity of the estimated local PSF. Figure 6-2 shows that the use of adaptive limited support increases the image quality of the estimated object.

Adaptation to Point of Maximum Intensity

A second approach is to make the centre of limited support region equal to the point of maximum intensity of the estimated PSF. The same experiment was performed. In a first simulation TIP3A was used without adaptive limited support and the adaptive limited support was turned on during the second simulation. Figure 6-3 shows that using the point of maximum intensity as the centre of the adaptive limited support region does not increase the image quality of the estimated object.

The outcome of this section is that adaptive limited support where the centre of the limited support area is set to the centre of gravity of the estimated PSF increases the image quality of the estimated object. Figure 6-2 shows an example of an experiment where the FRC of the estimated object has improved from 0.45 to 0.75 by using adaptive limited support. TIP3A with adaptive limited support called TIP4A.

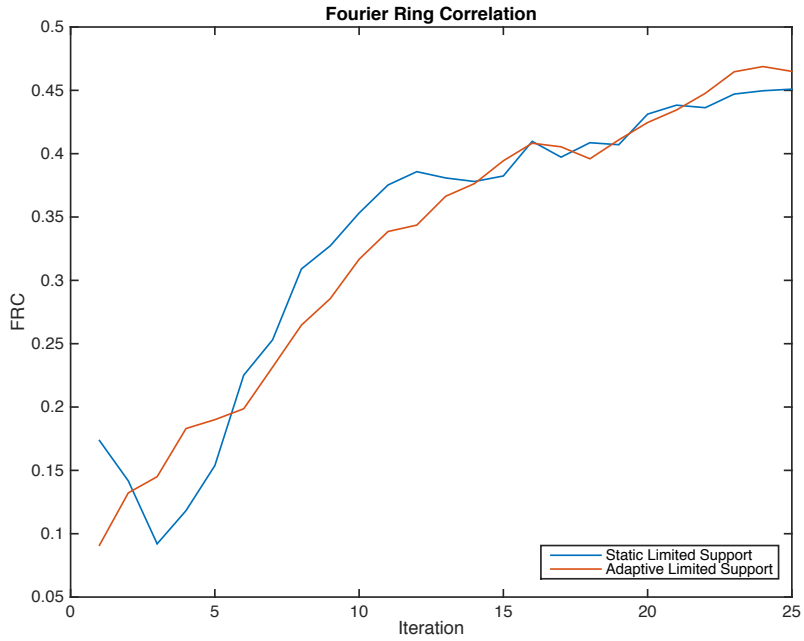

Figure 6-3: The image quality of the estimated object over 25 iterations, measured with FRC. In this figure can be seen that adaptive limited support with the centre of the limited support region set to the point of maximum intensity of the estimated PSF, does not increase the image quality of the estimated object.

6-2 Fourier Domain Modification

TIP3A and TIP4A are designed for images that are locally the result of convolution. This model is closer to nature than assuming one global PSF, especially in deep tissue microscopy. However, in highly anisoplanatic imaging systems, the image model that assumes local convolution between the object and local PSF, can be violated.

For computationally efficient deconvolution algorithms, this assumption is of immense importance. Assuming local convolution in the images, allows the use of local deconvolution in the Fourier domain. Deconvolution in the Fourier domain is performed via the Fast Fourier Transform, a computationally efficient approach to deconvolution.

In order to design a computational approach that is yet in the line of local deconvolution in the Fourier domain, it is favorable that images are truly the result of local convolution. As this assumption might be violated for some image subsection, it can still be a very good approximation on others. This motivates the use of weighted multi-frame deconvolution.

6-2-1 Weighted Multi-Frame Deconvolution

This novel approach to multi-frame deconvolution uses isoplanatic weights, $a_{p,q|s} \in [0, \infty)$, to measure the level of isoplanatism in the image. If the image subsection within the apodization region is isoplanatic the weight is large, if the PSF is space-variant the the weight is small. The way these weights are determined is described in the next section.

The estimated object subsection by weighted multi-frame linear deconvolution in the Fourier domain is given by

$$\bar{o}_{p,q}^{(k)} = \mathcal{F}^{-1}\left\{ \frac{\sum_{s=1}^{S} a_{p,q|s} \left(H_{p,q|s}^{(k)}\right)^{*} I_s}{\sum_{s=1}^{S} a_{p,q|s} |H_{p,q|s}^{(k)}|^2} \right\}. \tag{6-1}$$

6-2-2 Measuring Isoplanatism in Images

The weights, $a_{p,q|s}$, reflect the level of isoplanatism, or PSF variation, in an image subsection $i_{p,q|s}$. To determine the PSF variation in the image subsection ,$i_{p,q|s}$, the estimated local PSF, $h_{p,q|s}$, is used. The estimated local PSF depends on the apodization kernel that is applied on the object. The object subsection is determined by multiplication of the object with an apodization kernel. The width of this kernel influences the estimated local PSF. As the estimated local PSF represents the SV PSF in the object subsection, the estimated local PSF changes when the apodization is changed. If the variation in the SV PSF is small, the estimated local PSF is less variant under changes in the apodization. On the other hand, when the variation in the SV PSF is large, the local estimated PSF changes much more with changes in the apodization.

Let $K_{p,q}$ be the apodization kernel for object subsection, $o_{p,q}$, and $h_{p,q|s}$ is the estimated local PSF as a result of the kernel, $K_{p,q}$. Similarly, let $\tilde{K}_{p,q}$ be a larger apodization kernel and $\tilde{h}_{p,q|s}$ the corresponding estimated local PSF. $K_{p,q}$ and $\tilde{K}_{p,q}$ are chosen initial to the algorithm. $K_{p,q}$ is only dependant on the apodization width w and $\tilde{K}_{p,q}$ can be calculated from $w + \Delta w$. The local PSF variation is represented by

$$a_{p,q|s}(h_{p,q|s}, \tilde{h}_{p,q|s}). \tag{6-2}$$

PSF Variation

The PSF variation is a measurement for the difference or distance between the estimated local PSF, $h_{p,q|s}$, and local complementary PSF, $\tilde{h}_{p,q|s}$. This measurement must be chosen, such that the image quality of the estimated object is optimized. This thesis mainly shows PSF variation is a good approach to weighted multi-frame deconvolution. Optimizing a metric for PSF variation is still an open question.

In this thesis, three basic metrics are considered to determine the weights, $a_{p,q|s}$. Other measurements are derived from from these three. The three basic metrics are chosen such that $b_i \in [0, 1]$. If the metric is zero the estimated local PSF does not overlap the local complementary PSF. When both PSFs are equal, the image is locally isoplanatic and the metric will be 1.

The first metric is the Bhattacharyya coefficient, that is used in patter recognition [39]. The first metric is given by

$$b_1 = \sum \sqrt{h_{p,q|s} \tilde{h}_{p,q|s}}, \tag{6-3}$$

where is sum is taken over all pixels. The second metric is a linear mapping from the total absolute error to the interval $[0, 1]$.

$$b_2 = 1 - \frac{1}{2} ||h_{p,q|s} - \tilde{h}_{p,q|s}||_1 \tag{6-4}$$

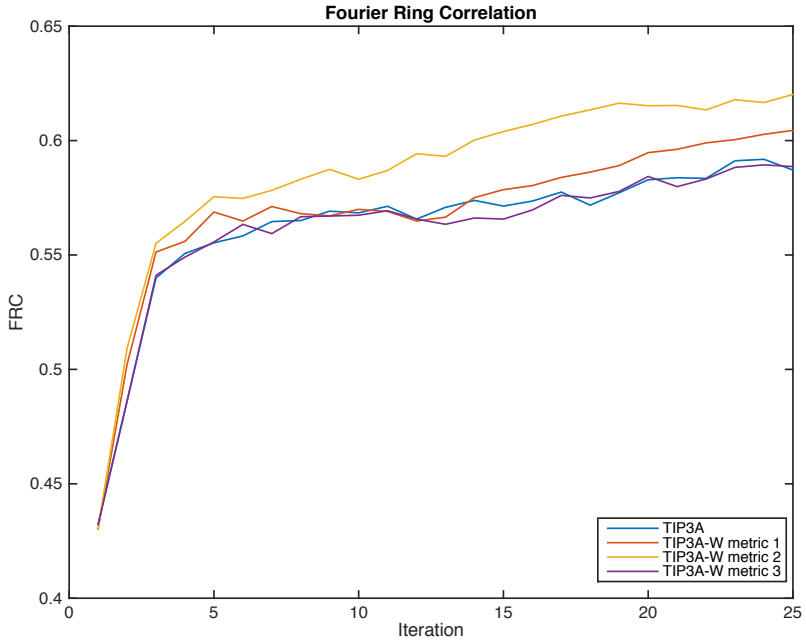

Figure 6-4: The image quality of the estimated object over 25 iterations, measured with FRC. This figure shows a comparison between TIP3A and TIP3A-W with 3 different metrics for the PSF variation. Metric 1 is given by $b_1 = \sum \sqrt{h_{p,q|s} \tilde{h}_{p,q|s}}$, metric 2 is given by $b_2 = 1 - \frac{1}{2}||h_{p,q|s} - \tilde{h}_{p,q|s}||_1$ and metric 3 is given by $b_3 = 1 - \frac{1}{4}||h_{p,q|s} - \tilde{h}_{p,q|s}||_2^2$.

Finally, the last metric is a linear mapping from the total squared error to the interval $[0, 1]$.

$$b_3 = 1 - \frac{1}{4}||h_{p,q|s} - \tilde{h}_{p,q|s}||_2^2 \tag{6-5}$$

6-2-3 Results

Weighted multi-frame deconvolution was applied in an experiment. TIP3A with weighted multi-frame deconvolution, denoted by TIP3A-W, was used in a simulation. The algorithm parameters are $r_{\mathbb{X}} = 6$, $\epsilon = 10^{-4.4}$, $w = 2000$ and $M = N = 7$. First the algorithm was conducted with the images in Appendix C with white Gaussian noise having a standard deviation $\sigma = 10^{-5}$. The weights, $a_{p,q|s}$, are given by the basic metrics, b_i. The results are given in Figure 6-4. Another result is that TIP3A-W requires more input images than TIP3A for convergence. The same experiment was conducted with the first 10 images in Appendix C. TIP3A-W did not converge with 10 input images.

The sensitivity of the basic metrics can be increased. This can be done by remapping of the basic metrics, b_i, to the more sensitive metrics. Here was chosen for remapping in two different ways. The first remapping is performed by the natural logarithm, $m_i = -\log(1 - b_i)$. The same experiment was repeated and the results are shown in Figure 6-5.

The second method of mapping the basic metric, b_i, is done via the multiplicative inverse. Let the metric $\bar{m}_i = \frac{1}{1-b_i}$. The main difference between mapping via the natural logarithm

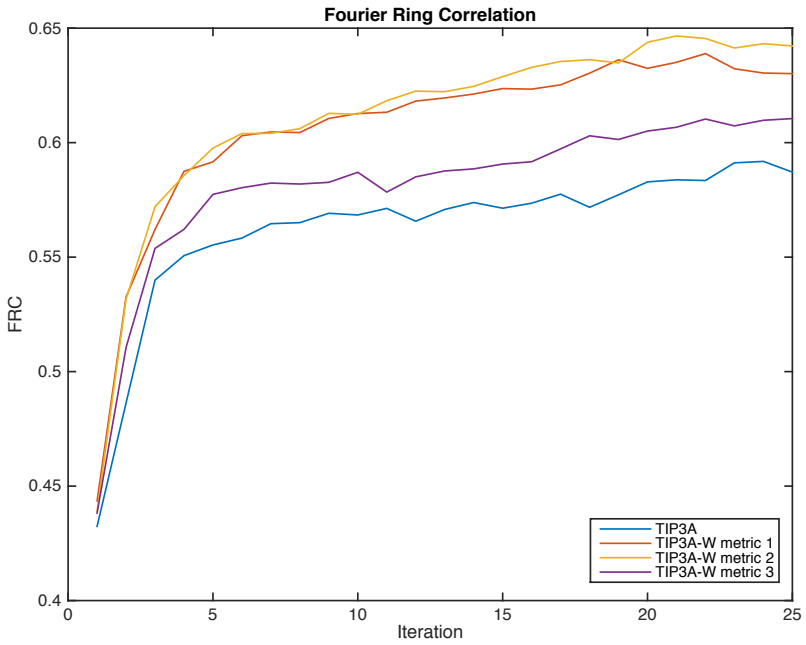

Figure 6-5: The image quality of the estimated object over 25 iterations, measured with FRC. This figure shows a comparison between TIP3A and TIP3A-W with 3 different metrics for the PSF variation. Metric 1 is given by m_1, metric 2 is given by m_2 and metric 3 is given by m_3, where $m_i = -\log(1 - b_i)$.

and mapping via the multiplicative inverse is that $m_i \in [0, \infty)$ and $\bar{m}_i \in [1, \infty)$. The results are shown in Figure 6-6

The choice of the metric for the PSF variation influences the image quality of the estimated object significantly. In Figure 6-4 can be seen that metrics b_2 and b_3 will result in almost similar image quality. However, in Figure 6-6 can be seen that for all metrics $\bar{m}_i$ the image quality from 0.58 to $0.65 - 0.70$. To put this result into perspective, the image quality was 0.71 after 25 iteration in TIP4A for the same input images and global algorithm parameters. On the other hand, TIP3A-W is of order 10 times faster than TIP4A.

It is possible to achieve better image quality with further tuning of the metrics. Figure 6-7 shows the results after the same simulation as in Figure 6-6, only metric 3 was raised to the power, $p_s = 1.5$, and $a_{p,q|s}$ was set to zero if it was under a threshold, $tr = 20$. The metric is then given by $\bar{m}_3^* = (1 - b_3)^{-1.5}$, $\bar{m}_3^* = 0$ if $\bar{m}_3 < 20$.

6-3 TIP4A-W

Naturally, a new algorithm is formed when TIP3A is modified with both adaptive limited support and weighted multi-frame deconvolution. This modified algorithm is called TIP4A-W. It was hypothesized that TIP4-W would outperform TIP4A and TIP3A-W. In order to demonstrate the performance of TIP4A-W, the same experiment as in Section 6-2 was conducted with the addition of adaptive limited support.

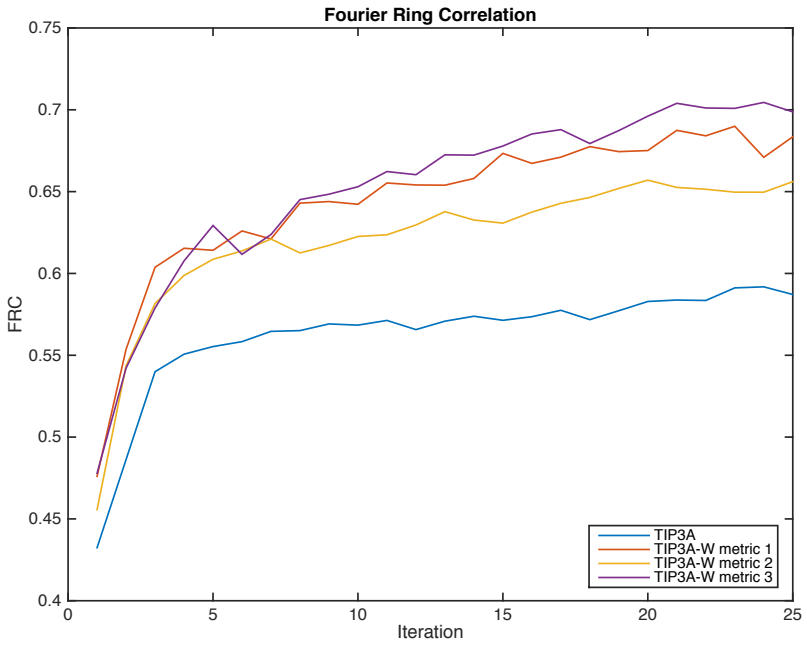

Figure 6-6: The image quality of the estimated object over 25 iterations, measured with FRC. This figure shows a comparison between TIP3A and TIP3A-W with 3 different metrics for the PSF variation. Metric 1 is given by $\bar{m}_1$, metric 2 is given by $\bar{m}_2$ and metric 3 is given by $\bar{m}_3$, where $\bar{m}_i = \frac{1}{1-b_i}$.

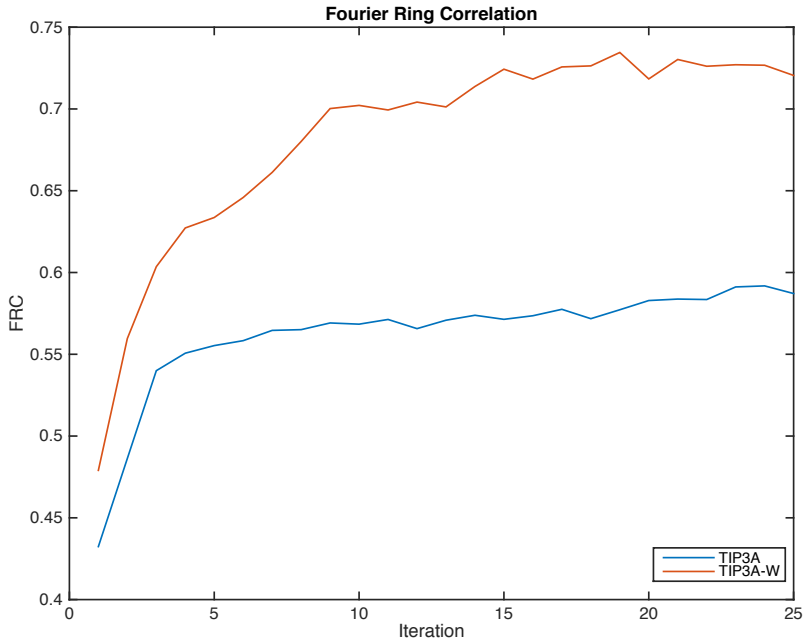

Figure 6-7: The image quality of the estimated object over 25 iterations, measured with FRC. This figure shows a comparison between TIP3A and TIP3A-W with metric given by $\bar{m}_3^*$.

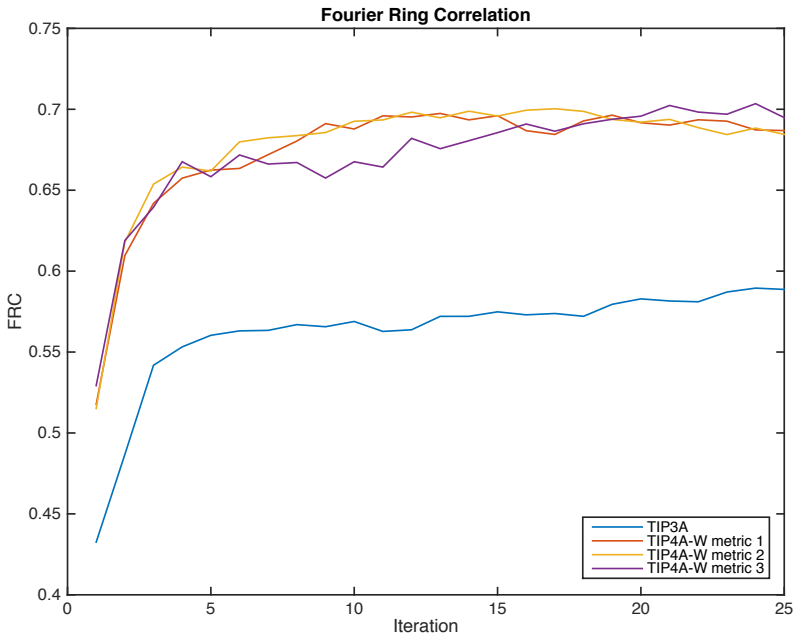

Figure 6-8: The image quality of the estimated object over 25 iterations, measured with FRC. This figure shows a comparison between TIP3A and TIP4A-W with 3 different metrics for the PSF variation. Metric 1 is given by m_1, metric 2 is given by m_2 and metric 3 is given by m_3, where $m_i = -\log(1 - b_i)$.

6-3-1 Results

Figure 6-8 shows the result of an experiment where the same three basic metrics, b_i, as in Figure 6-4 are used. Metrics b_i are given in Equations (6-3), (6-4) and (6-5). Comparing Figure 6-8 with Figure 6-4 shows that for the basic metrics TIP4A-W is superior to TIP3A-W in this experiment.

When three other, more sensitive, metrics are used, it is expected that the image quality of the estimated object becomes better. Similar to the experiment in Section 6-2, the sensitivity of the basic metrics, b_i, is increased by remapping into three mew metrics, $m_i = -\log(1-b_i)$. The result of this experiment is given in Figure 6-9. Compare this to the result in Figure 6-5, it can be seen that TIP4A-W with metrics, m_i, performs better than TIP3A-W. Figure 6-9 also shows that TIP4A-W with metric, b_2, performs equal to TIP4A with similar input images. Both TIP4A-W and TIP4A achieve an FRC of0.71 after 25 iterations.

During the experiment in Section 6-2, the metric ,$\bar{m}_i = \frac{1}{1-b_i}$, performed the best. Figure 6-10 shows the result of TIP4A in combination with metrics, $\bar{m}_i$. In this figure can be seen that the results with TIP4A-W are better than the results shown in Figure 6-6, where TIP4A was used.

The best result was found after tuning the parameters of TIP4A. Metric 3 was selected for measuring the PSF variation. This metric was changed by two parameters. Tuned metric 3 is given by

$$\bar{m}_3^* = \left(\frac{1}{4}||h_{p,q|s} - \tilde{h}_{p,q|s}||_2^2\right)^{-p_s}, \qquad \bar{m}_3^* = 0 \quad \text{if} \quad \bar{m}_3 < tr. \tag{6-6}$$

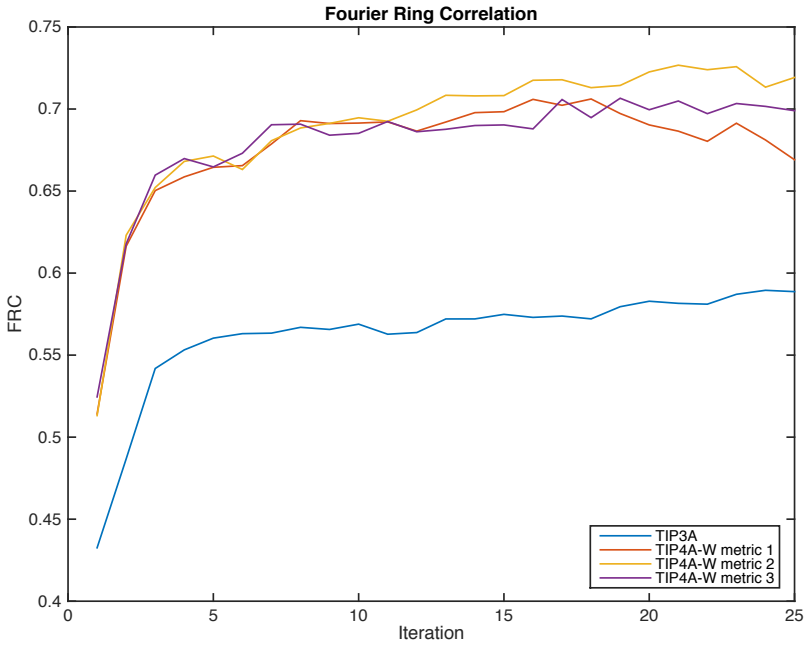

Figure 6-9: The image quality of the estimated object over 25 iterations, measured with FRC. This figure shows a comparison between TIP3A and TIP4A-W with 3 different metrics for the PSF variation. Metric 1 is given by m_1, metric 2 is given by m_2 and metric 3 is given by m_3, where $m_i = -\log(1 - b_i)$.

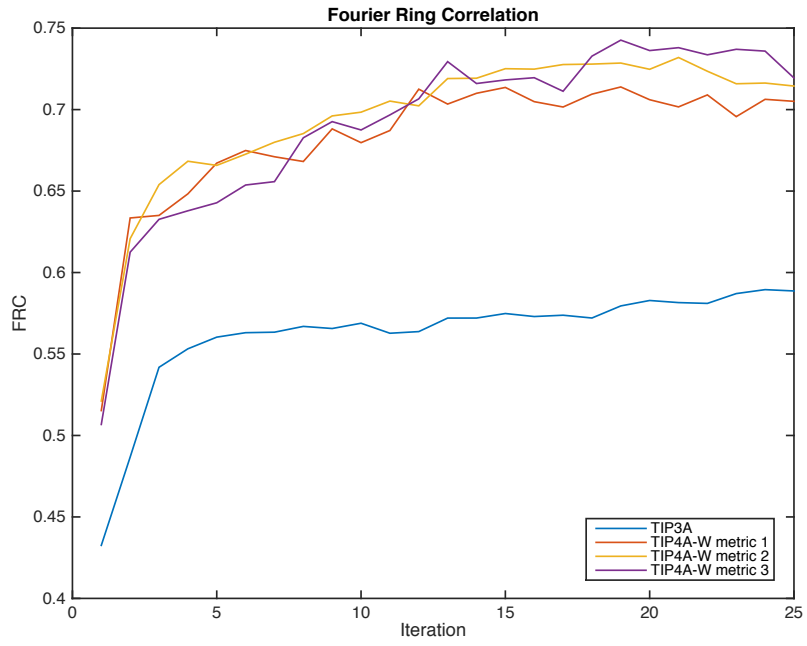

Figure 6-10: The image quality of the estimated object over 25 iterations, measured with FRC. This figure shows a comparison between TIP3A and TIP4A-W with 3 different metrics for the PSF variation. Metric 1 is given by $\bar{m}_1$, metric 2 is given by $\bar{m}_2$ and metric 3 is given by $\bar{m}_3$, where $\bar{m}_i = \frac{1}{1-b_i}$.

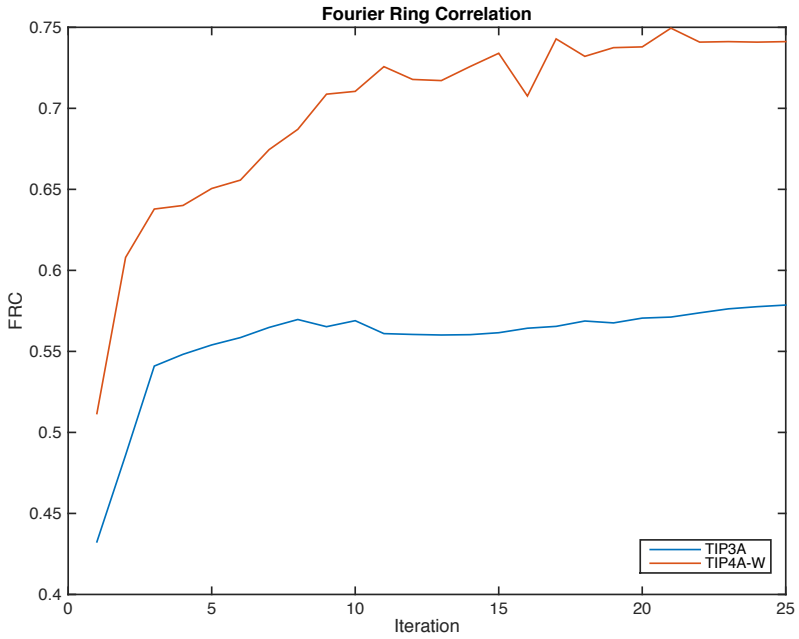

Figure 6-11: The image quality of the estimated object over 25 iterations, measured with FRC. This figure shows a comparison between TIP3A and TIPWA-W with metric given by $\bar{m}_3^*$.

After tuning was found that $p_s = 1.5$ and $tr = 5$. The image quality of the estimated object over 25 iteration is given in Figure 6-11.

6-3-2 Experiments with Additional Noise

In the experiments with TIP4A-W in the previous section, noise was added to the images. The pixels in the images have a range from 0 to 1 and the additional Gaussian white noise in the images has standard deviation $\sigma = 10^{-5}$. The simulation with TIP4A-W and tuned metric, $\bar{m}_3^*$, was repeated with different noise levels. Table 6-1 shows the image quality of the estimated object measured with Fourier ring correlation (FRC) and structural similarity (SSIM) after 25 iterations of TIP4A-W. The effects of noise on the image quality is represented by the decreasing value of the SSIM as the noise increases.

Table 6-1: Image quality of the estimated object after 25 iterations of TIP4A-W using tuned metric $\bar{m}_3^*$ for the PSF variation. White Gaussian noise with different standard deviations (st. dev.) was added to the set of images. The image quality is measured with FRC and SSIM.

Noise st. dev.	$\sigma = 10^{-5}$	$\sigma = 10^{-4}$	$\sigma = 10^{-3}$	$\sigma = 10^{-2}$	$\sigma = 10^{-1}$
FRC	0.74	0.73	0.72	0.72	0.72
SSIM	0.55	0.55	0.54	0.33	0.08

The estimated objects after 25 iterations for a set of input images with different standard deviation are shown in Figure 6-12. The images from left to right are the result of TIP4A-W with input images with addition white Gaussian noise with increasing standard deviation.

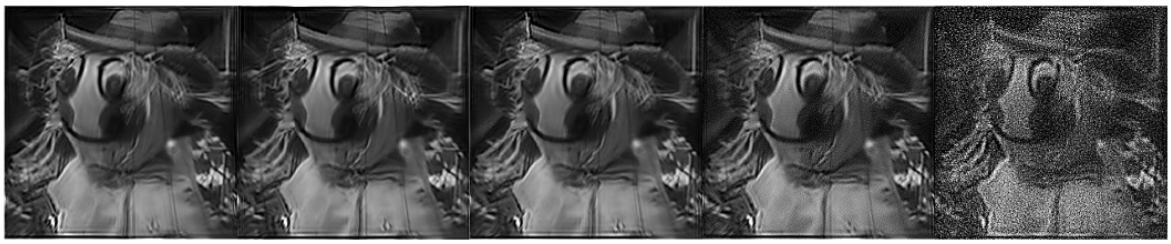

Figure 6-12: In an experiment TIP4A-W was used to estimate the original object from sets of input images with different noise levels. White Gaussian noise with varying standard deviations, $\sigma = 10^{-5}, 10^{-4}, 10^{-3}, 10^{-2}, 10^{-1}$, was added to the images. The estimated object corresponding to the sets of input images with different noise levels are depicted in this figure. The quality of the estimated objects can be found in Table 6-1 in the same order.

6-3-3 Experiments with Real Images

The performance of TIP4A-W was tested on a set of real images. 40 image with unknown aberrations were acquired and TIP4A-W was used to improve the image quality. In this experiment the aberrations are not simulated and the scientific object is unknown. Therefore, it is not possible to compare the result of TIP4A-W with a ground truth. In this experiment a sharpness metric will be used to compare the performance of TIP4A-W with the performance op TIP3A and TIP. Let the sharpness of a normalized image, $\bar{i}$, be

$$I^2 = \sum \bar{i}^2, \tag{6-7}$$

where the sum is over all pixels.

In the experiment 25 iterations of each algorithm was run. One of the initial images is shown in Figure 6-13. The sharpness of the initial images is approximately $I^2 = 6.29 \cdot 10^{-5}$. After 25 iterations of TIP, TIP3A and TIP4A-W the sharpness of the estimated object was calculated again. The results are shown in Table 6-2 and the estimated object with TIP4A-W is given in Figure 6-14.

According to the sharpness metric the image quality has improved with only 1% when TIP4A-W is used, however the optimum value for the sharpness or the sharpness of the true object is unknown. From a visual comparison between Figure 6-13 and Figure 6-14 can be concluded that some of the details that were not visible in the original image are visible in the estimated object with TIP4A-W. Comparing the contrast, especially on the left side in both images, it can be seen that three adjacent lines are more distinguishable. Even the smaller lines are now more separated and are visible as individual lines.

Table 6-2: The performance of TIP, TIP3A and TIP4A-W is compared in an experiment. The image quality given by the sharpness metric.

Image	**original**	**TIP**	**TIP3A**	**TIP4A-W**
I^2	$6.29 \cdot 10^{-5}$	$6.31 \cdot 10^{-5}$	$6.31 \cdot 10^{-5}$	$6.34 \cdot 10^{-5}$

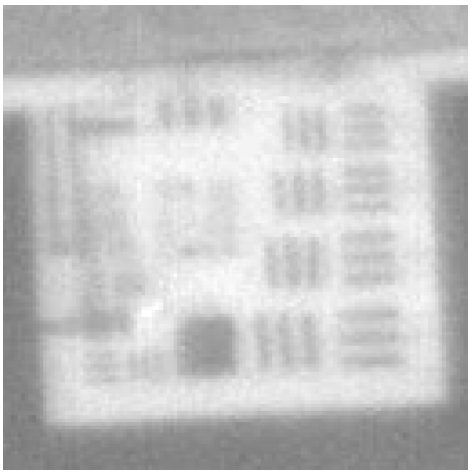

Figure 6-13: One of the obtained images that was used as an input for the TIP4A-W algorithm during an experiment with real images. The aberrations in this image are unknown. Moreover, the scientific object is unknown. The sharpness of the normalized image as given by Equation (6-7) is given $I^2 = 6.29 \cdot 10^{-5}$.

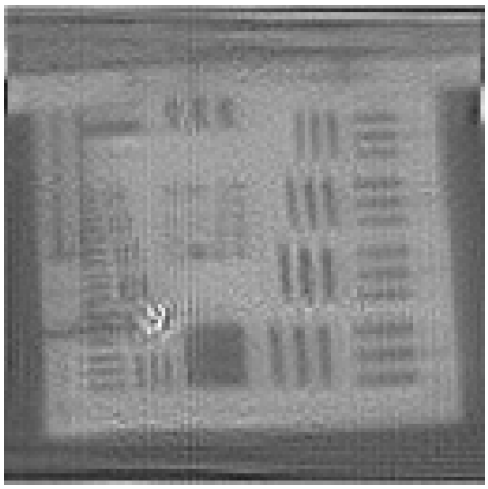

Figure 6-14: The estimated object given after 25 iteration of TIP4A-W is shown in this figure. The image quality given by the sharpness, Equation (6-7), has improved by only 1%. The sharpness of this image is $I^2 = 6.35 \cdot 10^{-5}$

6-3-4 Algorithm Comparison

The performance of TIP4A-W was compared to a method by Hirsch *et al.* [11]. Three experiments were conducted to perform this comparison. In the first experiment the images in Appendix A are used as an input for TIP4A-W and the method by Hirsch *et al.* [11]. In the second experiment the images in Appendix C are used as an input for both algorithms. For the third experiment, astronomical images provided in [11] were used an an input for both algorithms.

Results

The images in Appendix A have anisoplanatic aberrations. They are used as an input for TIP4A-W and the method by Hirsch *et al.* [11]. Figure 6-15 shows the estimated object given by the method in [11]. The estimated object after 40 iterations of TIP4A-W is shown in Figure 6-16. Comparing both results in Figures 6-15 and 6-16 it can seen that the reconstruction for TIP4A-W is sharper. Details in the straw hair or in puppet's Collar are more visible in the TIP4A-W reconstruction than in the reconstruction by Hirsch *et al.*.

The images in Appendix C show large aberration, especially in the form of morph. The method in [11] was used to estimate the true object from the images in Appendix C, the result is given in Figure 6-17. Furthermore, 40 iterations of TIP4A-W were used in order to estimate the object. Figure 6-18 shown the results of TIP4A-W with the images in Appendix C as input. This experiment demonstrates that TIP4A-W can handle large anisoplanatic

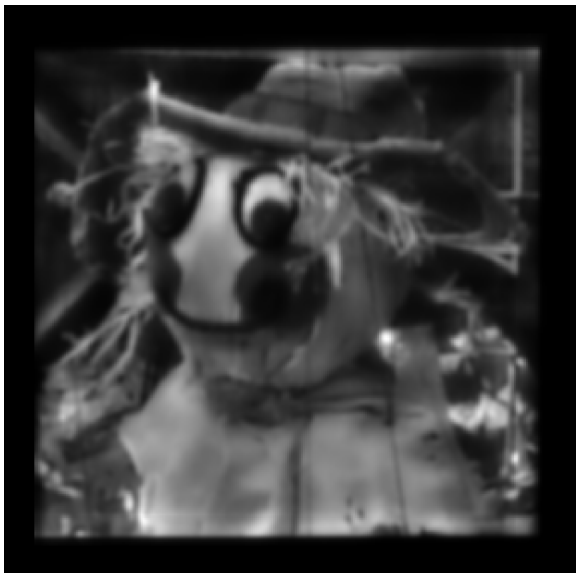

Figure 6-15: The estimated object given by the method of Hirsch *et al.* [11]. The images in Appendix A were used as input.

Figure 6-16: The estimated object after 40 iterations of TIP4A-W with the images in Appendix A as input.

aberrations. When Figure 6-18 is compared to Figure 6-17 it becomes clear that TIP4A-W can handle anisoplanatic aberrations much better.

A set of 40 astronomical images were provided in [11]. One of these images is shown in Figure 6-19. Figure 6-20 shows the estimated object given by the method of Hirsch *et al.* for the set of astronomical images. The object was also estimated by TIP4A-W. The result after 40 iterations of TIP4A-W is given in Figure 6-21. Comparing Figure 6-20 with Figure 6-21 can be seen that for these astronomical images the method by Hirsch *et al.* performs better than TIP4A-W.

6-3-5 Discussion

Since TIP4A-W and the other TIP-based algorithms use TIP for local deconvolution. Some of the limitations of TIP are directly related to the limitations of these algorithms. Wilding *et al.* [3] describe that TIP does not fit into a mathematical framework yet. The results are observed in experiments and the convergence of the algorithm was shown empirically.

TIP was designed for situations where the signal-to-noise ratio is low and where temporal dynamics of the aberrations is much faster than the object's. This limitation also holds for the TIP-based algorithms described in this thesis. Temporal dynamics are important because more than one image is required for these kind of algorithms.

Optimal performance of the algorithm can be achieved when the sum of local PSF spectra covers all frequency within the bandlimit of the system. In practice it is favorable to collect as much images of the same static object as possible, while the aberrations are induced by the environment. Furthermore, when only a part of the aberrations is dynamic and some of the aberrations are static, TIP-based algorithms are not able to remove the static aberration from the images.

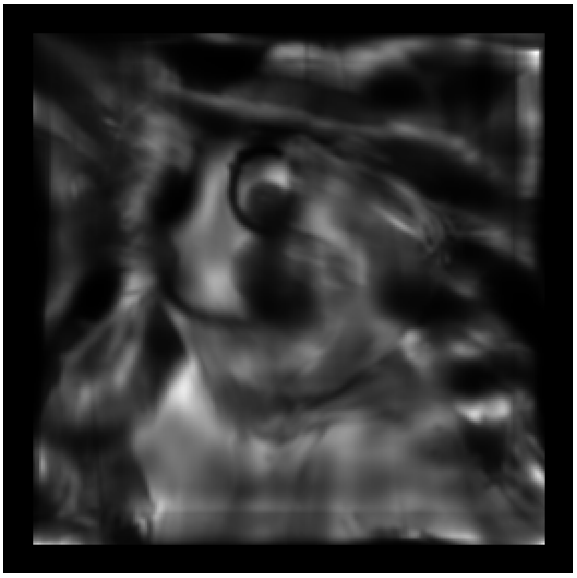

Figure 6-17: The estimated object given by the method of Hirsch *et al.* [11]. The images in Appendix C were used as input.

Figure 6-18: This image is the result after 40 iterations of TIP4A-W with the images in Appendix C as input.

Figure 6-19: One of the forty input images provided by Hirsch *et al.* [11].

Figure 6-20: The estimated object given by the method of Hirsch *et al.* [11] with the images provided in [11] as input.

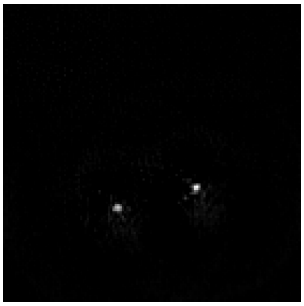

Figure 6-21: This image is the result after 40 iterations of TIP4A-W with the images provided in [11] as input.

Especially when the aberrations are anisoplanatic it is highly favorable to use as many images as possible. TIP3A-W and TIP4A-W are designed specifically to use parts of the image where the PSF variation is low. In other words, local regions with almost isoplanatic aberrations are used to calculate the estimated object. When more images are collected it is more likely for such regions to occur.

In TIP3A-W and TIP4A-W PSF variation is used to calculate the weights for weighted multi-frame deconvolution. It was only shown empirically that PSF variation improves the image quality when an adequate metric was used. It is unknown how PSF variation can be measured optimally in a sense that the image quality of the estimated object will be optimal. Moreover, PSF variation was only used to show the positive effect of weighted multi-frame deconvolution. Further research must be conducted to expand the theoretical knowledge about weighted multi-frame deconvolution.

Chapter 7

Conclusion and Future Outlook

Research has been conducted on correction methods for anisoplanatic aberrations. In living biological tissue the phase aberrations are time-variant and anisoplanatic. This thesis shows the development of an algorithm that can handle these type of aberrations. Despite the fact that this algorithm is so innovative, the algorithm can still be improved.

7-1 Conclusion

It was discovered in literature study that local deconvolution in an efficient filter flow framework [6] is a computational efficient approach to blind deconvolution of anisoplanatic aberrations. As this computational efficiency comes with a small cost in model accuracy, a robust algorithm was selected to perform local deconvolution. Tangential iterative projections (TIP) [3] is fast and robust algorithm that was designed specifically for situations where the aberrations are time-variant.

Tangential iterative projections algorithm for anisoplanatic aberrations (TIP3A) is a new method where TIP is applied to the computational efficient framework. The estimated object is formed by interpolation of local results. Local deconvolution is performed by TIP. Thereafter, the results are interpolated similar to the ideas in [6, 7, 5].

Since TIP was designed to handle time-variant, but space invariant point spread functions (PSF), it was expected that TIP3A can handle time- and space-variant aberrations better. The metrics Fourier ring correlation (FRC) and structural similarity (SSIM) were able to show that in situations where the PSFs were space-variant, indeed TIP3A outperformed TIP.

Furthermore, during research was discovered that modifications can be made in both the spatial domain and the Fourier domain. It was shown that adaptive limited support in the spatial domain increases the image quality of the estimated object.

Moreover, the Fourier domain modification called weighted multi-frame deconvolution has shown to improve image quality of the estimated object. This novel approach was applied in conjunction with PSF variation.

Both modification have resulted in new algorithms. The addition of adaptive limited support to TIP3A forms a new algorithm called tangential iterative projections algorithm for anisoplanatic aberrations with adaptive limited support (TIP4A). The Fourier domain modification called weighted multi-frame deconvolution can be added to both TIP3A and TIP4A resulting in two new algorithms called TIP3A-W and TIP4A-W respectively.

In addition, a whole different approach was researched. This research has not lead to the development of a new algorithm. More information about this approach can be found in Appendix D.

7-2 Future Outlook

The next step in this research might take the global algorithm parameters to local algorithm parameters. Global parameters such as limited support radius, $r_{\mathbb{X}}$, threshold of division, ϵ, and apodization width, w, can be considered as local parameters. Tuning those parameters for every object subsection individually can be a task for an artificial intelligence.

In the current state of the algorithms, the object subsections are distributed on an M by N rectangular. This might, however, not be the most optimal distribution. Furthermore, the object subsections do not have to be all the same size. Finding the optimal object subsection distribution and size, combined with finding optimal local parameters, is a task that can be performed by an artificial intelligence.

In this research weighted multi-frame deconvolution is applied in conjunction with PSF variation. It was shown that this modification improves the image quality of the estimated object. However, weighted multi-frame deconvolution is a novel approach that should be researched further for optimal results. Moreover, in weighted multi-frame deconvolution constant weights, $a_{p,q|s}$, are used, it is possible that matrix weights must be used for optimal performance.

ϵ, the threshold of division was also considered a constant during this research. As the error in the image model is more likely to be larger at the edges of an image subsection, it is possible that using a non-constant threshold of division performs better.

Al the algorithms developed in this thesis use the shape of the local PSFs for reconstruction of the underlying physical object. A next step in this research could include the phase aberration. Assuming a single conjugation plane outside the pupil plane leads to a phase retrieval problem. Explicit use of the anisoplanatic phase aberration might lead to more coherence between the local PSFs.

Appendix A

Images with Anisoplanatic Aberrations

The images in Figure A-1 are used in section 4-2-2. These images are used an a set of input images for TIP and TIP3A with varying number of subsections.

The projection method as shown in Figure 2-3 with a single phase screen was used to calculate the SV phase aberration. A phase plane is placed at distance l_1 to the right of the object plane. The pupil plane is at distance l_2 tot he right of the phase plane. Therefore, the object distance $z_o = l_1 + l_2$. A thin lens is with numerical aperture, NA, is located in the pupil.

A phase screen, ϕ, is placed in the phase plane. This phase screen is the sum of N_Z Zernike polynomials with maximum amplitude A_Z

$$\phi = A_Z \sum_{N=1}^{N_Z} a_N Z_N, \tag{A-1}$$

where $-1 < a_N < 1$ is a random number.

An object, Figure 4-4, was placed in the object plane. By geometry, the optical path from a point in the object to the pupil has an intersection plane in the phase plane. This intersection plane is unique for that point in the object. The phase aberration in the intersection plane is scaled in the x and y direction to fit exactly inside the pupil. As a result Equation (2-12) can be used to calculate the PSF. Equation (2-14) can be used to form the noiseless image with anisoplanatic aberrations.

In this Appendix 256 by 256 deteriorated images are formed. The imaging system's geometry is given by $l_1 = 2$, $l_2 = 3$, $NA = 0.7$. The Phase screens are given by $A_Z = 40$ and $N_Z = 40$. The set consists of 10 images for 10 random realizations of the phase screens.

Figure A-1: These images are used as input for TIP and TIP3A in section 4-2-2.

Appendix B

Results of Visual Experiments

The images in Appendix A are used as input images for TIP and TIP3A. The results of these algorithms are depicted in this Appendix. All figures display the estimated object after $1, 5, 10, 15, 20$ and 25 iterations, from left to right, top to bottom. In the caption of the images is described what algorithm was used and what the settings were during the experiment. These figures are used for visual comparison, to compare the performance of for different settings of the algorithms. A description of this experiment can be found in Section 4-2-2. The algorithm parameters are: Number of subsections, M, N, limited support radius, $r_{\mathbb{X}}$, apodization width, w and threshold of division, ϵ.

Figure B-1: Estimated object after $1, 5, 10, 15, 20$ and 25 iterations. The algorithm used is: TIP, $r_{\mathbb{X}} = 6$, $\epsilon = 10^{-4.4}$. Images with isoplanatic aberrations are used as an input here.

Figure B-2: Estimated object after $1, 5, 10, 15, 20$ and 25 iterations. The algorithm used is: TIP3A, $M = N = 1$, $r_{\mathbb{X}} = 6$, $w = 2000$, $\epsilon = 10^{-4.4}$. Images with isoplanatic aberrations are used as an input here.

Figure B-3: Estimated object after $1, 5, 10, 15, 20$ and 25 iterations. The algorithm used is: TIP3A, $M = N = 3$, $r_{\mathbb{X}} = 6$, $w = 2000$, $\epsilon = 10^{-4.4}$. Images with isoplanatic aberrations are used as an input here.

Figure B-4: Estimated object after $1, 5, 10, 15, 20$ and 25 iterations. The algorithm used is: TIP3A, $M = N = 7$, $r_{\mathbb{X}} = 6$, $w = 2000$, $\epsilon = 10^{-4.4}$. Images with isoplanatic aberrations are used as an input here.

Figure B-5: Estimated object after $1, 5, 10, 15, 20$ and 25 iterations. The algorithm used is: TIP3A, $M = N = 15$, $r_{\mathbb{X}} = 6$, $w = 2000$, $\epsilon = 10^{-4.4}$. Images with isoplanatic aberrations are used as an input here.

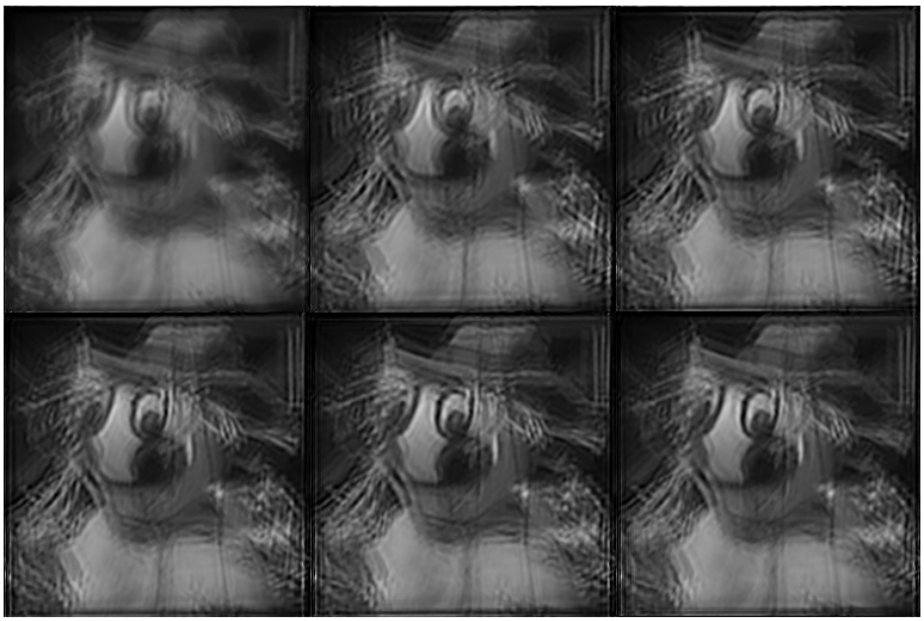

Figure B-6: Estimated object after $1, 5, 10, 15, 20$ and 25 iterations. The algorithm used is: TIP, $r_{\mathbb{X}} = 6$, $\epsilon = 10^{-4.4}$.

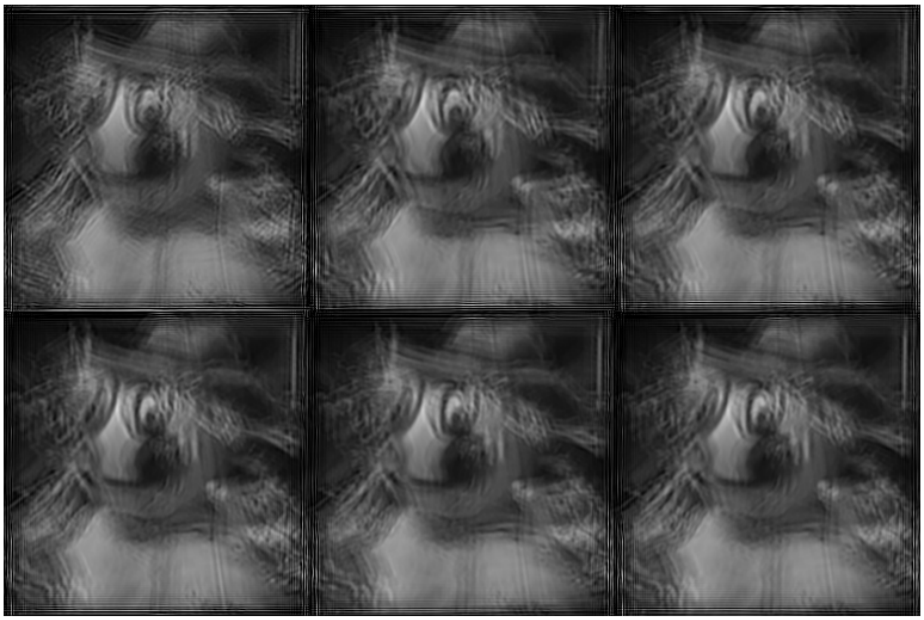

Figure B-7: Estimated object after $1, 5, 10, 15, 20$ and 25 iterations. The algorithm used is: TIP3A, $M = N = 1$, $r_{\mathbb{X}} = 6$, $w = 2000$, $\epsilon = 10^{-4.4}$.

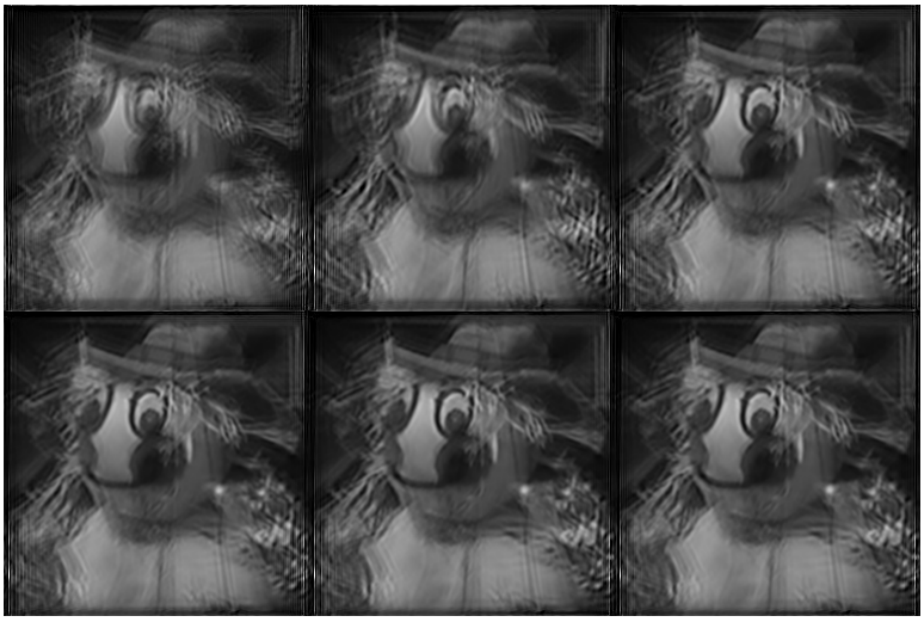

Figure B-8: Estimated object after $1, 5, 10, 15, 20$ and 25 iterations. The algorithm used is: TIP3A, $M = N = 3$, $r_{\mathbb{X}} = 6$, $w = 2000$, $\epsilon = 10^{-4.4}$.

Figure B-9: Estimated object after $1, 5, 10, 15, 20$ and 25 iterations. The algorithm used is: TIP3A, $M = N = 7$, $r_{\mathbb{X}} = 6$, $w = 2000$, $\epsilon = 10^{-4.4}$.

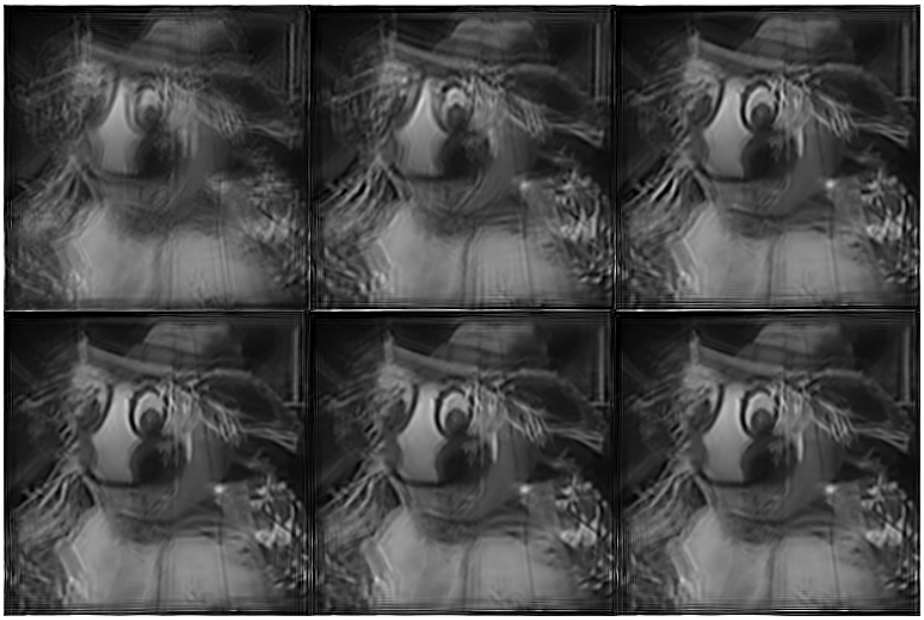

Figure B-10: Estimated object after $1, 5, 10, 15, 20$ and 25 iterations. The algorithm used is: TIP3A, $M = N = 15$, $r_{\mathbb{X}} = 6$, $w = 2000$, $\epsilon = 10^{-4.4}$.

Appendix C

Images with Anisoplanatic Aberrations

The images in Figure C-1 are used in section 6-2.

The projection method as shown in Figure 2-3 with a single phase screen was used to calculate the SV phase aberration. A phase plane is placed at distance l_1 to the right of the object plane. The pupil plane is at distance l_2 tot he right of the phase plane. Therefore, the object distance $z_o = l_1 + l_2$. A thin lens is with numerical aperture, NA, is located in the pupil.

A phase screen, ϕ, is placed in the phase plane. This phase screen is the sum of N_Z Zernike polynomials with maximum amplitude A_Z

$$\phi = A_Z \sum_{N=1}^{N_Z} a_N Z_N, \tag{C-1}$$

where $-1 < a_N < 1$ is a random number.

An object, Figure 4-4, was placed in the object plane. By geometry, the optical path from a point in the object to the pupil has an intersection plane in the phase plane. This intersection plane is unique for that point in the object. The phase aberration in the intersection plane is scaled in the x and y direction to fit exactly inside the pupil. As a result Equation (2-12) can be used to calculate the PSF. Equation (2-14) can be used to form the noiseless image with anisoplanatic aberrations.

In this Appendix 256 by 256 deteriorated images are formed. The imaging system's geometry is given by $l_1 = 1$, $l_2 = 3$, $NA = 0.7$. The Phase screens are given by $A_Z = 55$ and $N_Z = 40$. The set consists of 30 images for 30 random realizations of the phase screens.

Figure C-1: These images are used as input for TIP3A and TIP3A-W in section 6-2.

Appendix D

Blind Multi-Frame Anisoplanatic Deconvolution in a Higher Dimension

A blind multi-frame deconvolution (BMFD) method to estimate both object and space-variant point spread function is described. This method is based on conventional BMFD methods. However the conventional methods deal with a space invariant point spread function. Con-

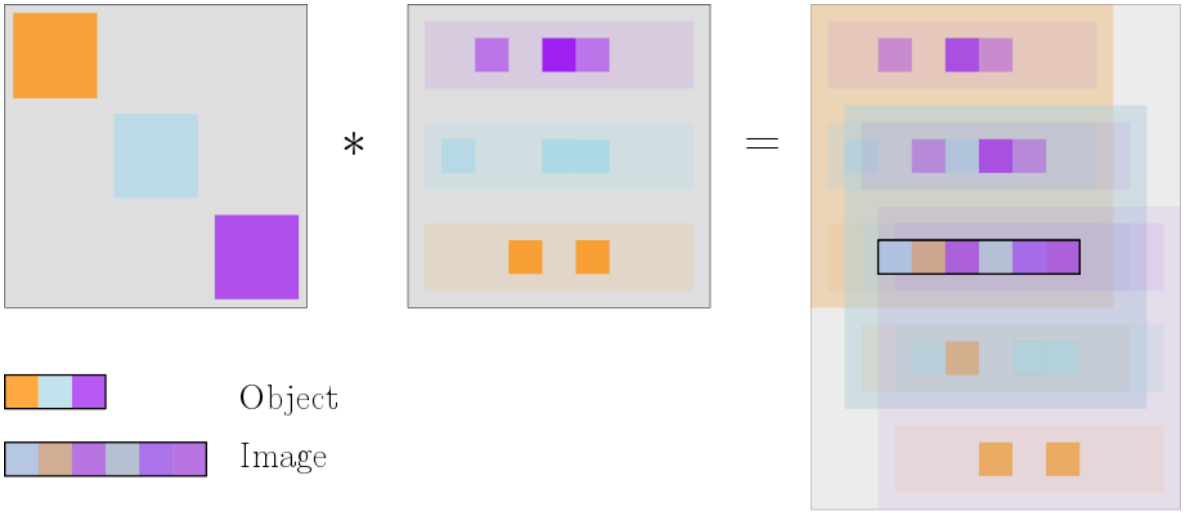

Figure D-1: Image formation is considered as a convolution of the object and point spread function. For a space-variant point spread function, image formation can still be considered to be a convolution, but in a higher dimension. Expansion of the 1D object to a diagonal matrix and stacking the 1D space-variant point spread function in reverse order, allows the computation of the 1D space-variant blurred image.

sider the discrete one dimensional extended object $o = [o_1, o_2, \cdots, o_n]$, where o_i are scalar intensities. Let $\mathcal{H}$ be the matrix containing point spread functions (PSF), h_i, corresponding

to the pixels o_i:

$$\mathcal{H} = \begin{bmatrix} h(o_n) \\ \vdots \\ h(o_2) \\ h(o_1) \end{bmatrix} \tag{D-1}$$

and Let $\mathcal{O}$ be the matrix containing object pixels on its diagonal:

$$\mathcal{O} = \begin{bmatrix} o_1 & 0 & 0 & 0 \\ 0 & o_2 & 0 & 0 \\ 0 & 0 & \ddots & 0 \\ 0 & 0 & 0 & o_n \end{bmatrix} \tag{D-2}$$

Then image formation with space-variant point spread function can be written as

$$\mathcal{I}_{i,j} = \sum_{k=1}^{n} \sum_{l=1}^{n} \mathcal{O}_{k,l} \mathcal{H}_{i-k,j-l}, \qquad i,j,k,l = 1,2,...,n. \tag{D-3}$$

Equation (3-2) can be recognized as a discrete convolution, demoted by $\mathcal{I} = \mathcal{O} * \mathcal{H}$. This calculation can be done very efficiently by application of the convolution theorem and the Fast Fourier Transform (FFT). The result of convolution is a matrix, $\mathcal{I}$, that contains the anisoplanatically deteriorated image in its nth row. Figure D-1 demonstrates the formation of a discrete image by convolution.

In the Fourier domain, Equation (3-2) can be written as

$$I_{i,j} = O_{i,j} H_{i,j} \tag{D-4}$$

where, capital letters denote the FFT of their corresponding ornamental letters in Equation D-3. In blind deconvolution H and O are unknown. Blind Multi-Frame Deconvolution (BMFD) uses S images and S corresponding PSFs. This leads to the minimization problem:

$$\{\hat{O}, \hat{H}_s\} = \arg\min_{H_s, O} \sum_{s=1}^{S} ||I_{i,j|s} - O_{i,j} H_{i,j|s}||^2, \tag{D-5}$$

where $||\cdot||$ represents the L_2 norm. This problem is conventionally solved by an alternating projection (AP) method. AP methods solve the equation for O from an initial PSF and then project the solution to a feasible set for all objects. Then the solution for H is calculated and projected on the feasible set of PSFs. This loop is iterated until convergence. In this method, an optimal solution to equation (D-5) was calculated with the same projections steps as in TIP [3].

In case of anisoplanatic aberrations, the extended image matrix $\mathcal{I}_{i,j}$ is not measured completely. The set of anisoplanatic images form the nth row in this matrix, therefore only the nth row is known. This problem was solved by simulating the unknown rows in $\mathcal{I}_{i,j}$ by convolution of the estimated object with the estimated space-variant PSF.

This method was implemented in MATLAB for $S = 1, S = 4$ and $S = 10$. Unfortunately, the algorithm did not converge to a solution. Figure D-2 shows the result of an experiment where 10 input images were used with anisoplanatic phase aberrations.

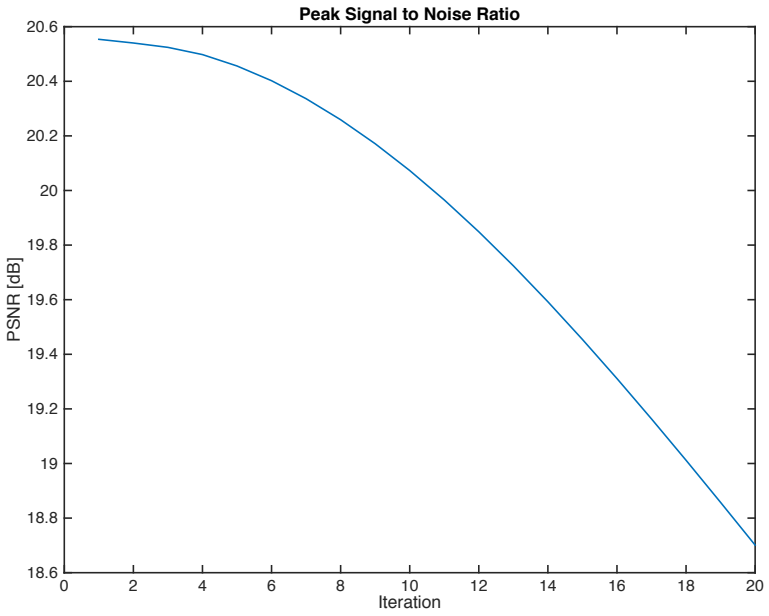

Figure D-2: The image quality of the estimated object measured with the PSNR is decreasing for this method. Here 10 images were used as input.

Bibliography

[1] C. P. Sreya Ghosh, "Three-dimensional block-based restoration integrated with wide-field fluorescence microscopy for the investigation of thick specimens with spatially variant refractive index," *Journal of Biomedical Optics*, vol. 21, pp. 21 – 21 – 14, 2016.

[2] D. Wilding, *Physical and Computational Approaches to Aberration Correction in Fluorescence Microscopy*. doctoral thesis, Delft University of Technology, 2018.

[3] D. Wilding, O. Soloviev, P. Pozzi, G. Vdovin, and M. Verhaegen, "Blind multiframe deconvolution by tangential iteravive projections," *Optics Express*, vol. 25, p. 32305, 2017.

[4] M. Verhaegen, P. Pozzi, O. Soloviev, G. Vdovin, and D. Wilding, "Control for high resolution imaging." Lecture Notes for the course SC42030, Tu Delft, 19 Apr 2017.

[5] J. G. Nagy and D. P. O'Leary, "Restoring images degraded by spatially-variant blur," *SIAM J. SCI. COMPUT*, vol. 19, pp. 1063–1082, 1997.

[6] L. Denis, E. Thiébaut, F. Soulez, J.-M. Becker, and R. Mourya, "Fast approximations of shift-variant blur," *International Journal of Computer Vision*, vol. 115, pp. 253–278, Dec 2015.

[7] M. Hirsch, S. Sra, B. Schölkopf, and S. Harmeling, "Efficient filter flow for space-variant multiframe blind deconvolution," in *IEEE Computer Society Conference on Computer Vision and Pattern Recognition*, pp. 607–614, Jun 2010.

[8] R. C. Flicker and F. J. Rigaut, "Anisoplanatic deconvolution of adaptive optics images," *J. Opt. Soc. Am. A*, vol. 22, pp. 504–513, March 2005.

[9] D. Miraut and J. Portilla, "Efficient shift-variant image restoration using deformable filtering (part i)," *EURASIP Journal on Advances in Signal Processing*, vol. 2012, Dec 2012.

[10] F. Sroubek, J. Kamenicky, and Y. M. Lu, "Decomposition of space-variant blur in image deconvolution," *IEEE Signal Processing Letters*, vol. 23, pp. 346–350, Mar 2016.

[11] M. Hirsch, S. Harmeling, S. Sra, and B. Schölkopf, "Online multi-frame blind deconvolution with super-resolution and saturation correction," *Astronomy & Astrophysics*, vol. 531, no. A9, 2011.

[12] D. Sage, L. Donati, F. Soulez, D. Fortun, G. Schmit, A. Seitz, R. Guiet, C. Vonesch, and M. Unser, "Deconvolutionlab2: An open-source software for deconvolution microscopy," *Methods*, vol. 115, pp. 28 – 41, 2017. Image Processing for Biologists.

[13] T.-w. Wu and M. Cui, "Numerical study of multi-conjugate large area wavefront correction for deep tissue microscopy," *Optics Express*, vol. 23, p. 7463, Mar. 2015.

[14] D. J. Griffiths, *Introduction to Electrodynamics*. Harlow, Edinburgh Gate: Pearson Education Limited, 4 ed., 2014.

[15] J. W. Goodman, *Introduction to Fourier Optics*. New York: The McGraw-Hill Companies, inc., 2 ed., 1996.

[16] R. J. Noll, "Zernike polynomials and atmospheric turbulence," *Journal of the Optical Society of America*, vol. A 66, pp. 207–211, 1976a.

[17] J. R. Fienup, "Phase retrieval algorithms: a personal tour *Invited*," *Applied Optics*, vol. 52, pp. 45–56, Jan 2013.

[18] T. P. Costello and W. B. Mikhael, "Efficient restoration of space-variant blurs from physical optics by sectioning with modified wiener filtering," *Digital Signal Processing*, vol. 13, no. 1, pp. 1 – 22, 2003.

[19] K. Andrews and B. Hunt, *Digital Image Restoration*. Englewood Cliffs, NJ: Prentice-Hall, 1977.

[20] D. Wilding, P. Pozzi, O. Soloviev, G. Vdovin, and M. Verhaegen, "Practical guidelines for implementing adaptive optics in fluorescence microscopy," *Proc.SPIE*, vol. 10502, pp. 10502 – 10502 – 12, 2018.

[21] C. W. Helstrom, "Image restoration by the method of least squares," *J. Opt. Soc. Am.*, vol. 57, pp. 297–303, Mar 1967.

[22] B. Gonzalez and R. woods, *Digital Image Processing*. New-York: Addison-Wesley, 1993.

[23] M. Cannon, "Blind deconvolution of spatially invariant image blurs with phase," *Acoustics, Speech and Signal Processing, IEEE Transactions on*, vol. 24, pp. 58 – 63, Mar 1976.

[24] S. Chaudhuri, R. Velmurugan, and R. Rameshan, *Blind image deconvolution: Methods and Convergence*. Cham: Springer, 2014.

[25] P. Campisi and K. Egiazarian, eds., *Blind image deconvolution: theory and applications*. Boca Raton: CRC Press, May 2007.

[26] R. W. Gerchberg and W. O. Saxton, "A practical algorithm for the determination of phase from image and diffraction plane pictures," *Optik*, vol. 35, pp. 237 – 246, 1972.

[27] G. Ayers and J. C. Dainty, "Iterative blind deconvolution method and its applications," *Optics letters*, vol. 13, pp. 547–549, 1988.

[28] T. J. Schulz, "Multiframe blind deconvolution of astronomical images," *J. Opt. Soc. Am. A*, vol. 10, pp. 1064–1073, May 1993.

[29] L. P. Yaroslavsky and H. J. Caulfield, "Deconvolution of multiple images of the same object," *Appl. Opt.*, vol. 33, pp. 2157–2162, Apr 1994.

[30] S. M. Seitz and S. Baker, "Filter flow," *IEEE 12th International Conference on Computer Vision*, pp. 143–150, 2009.

[31] L. Denis, E. Thiébaut, and F. Soulez, "Fast model of space-variant blurring and its application to deconvolution in astronomy," in *18th IEEE International Conference on Image Processing*, (Brussel, Belgium), pp. 2817–2820, Sep 2011.

[32] H. Trussell and B. Hunt, "Image restoration of space-variant blurs by sectioned methods," *IEEE Transactions on Acoustics, Speech, and Signal Processing*, vol. 26, pp. 196 – 198, may 1978.

[33] R. L. Lagendijk and J. Biemond, "Block-adaptive image identification and restoration," in *International Conference on Acoustics, Speech, and Signal Processing*, vol. 4, pp. 2497–2500, Apr 1991.

[34] Y. Guo, H. Lee, and C. Teo, "Blind restoration of images degraded by space-variant blurs using iterative algorithms for both blur identification and image restoration," *Image and Vision Computing*, vol. 15, no. 5, pp. 399 – 410, 1997.

[35] J. R. Fienup, "Invariant error metrics for image reconstruction," *Appl. Opt.*, vol. 36, pp. 8352–8357, Nov 1997.

[36] W. O. Saxton and W. Baumeister, "The correlation averaging of a regularly arranged bacterial cell envelope protein," *Journal of Microscopy*, vol. 127, no. 2, pp. 127–138, 1982.

[37] N. Banterle, K. H. Bui, E. A. Lemke, and M. Beck, "Fourier ring correlation as a resolution criterion for super-resolution microscopy," *Journal of Structural Biology*, vol. 183, no. 3, pp. 363 – 367, 2013.

[38] Zhou Wang, A. C. Bovik, H. R. Sheikh, and E. P. Simoncelli, "Image quality assessment: from error visibility to structural similarity," *IEEE Transactions on Image Processing*, vol. 13, pp. 600–612, Apr 2004.

[39] D. Comaniciu, V. Ramesh, and P. Meer, "Real-time tracking of non-rigid objects using mean shift," in *Proceedings IEEE Conference on Computer Vision and Pattern Recognition. CVPR 2000 (Cat. No.PR00662)*, vol. 2, pp. 142–149 vol.2, Jun 2000.

Glossary

List of Acronyms

PSF	point spread function
TIP	tangential iterative projections
FOV	field of view
FWHM	Full Width at Half Maximum
SV	space-variant
CCD	charge-coupled device
PSNR	peak signal-to-noise ratio
BMFD	blind multi-frame deconvolution
TIP3A	tangential iterative projections algorithm for anisoplanatic aberrations
MSE	mean squared error
NMSE	normalized mean squared error
FRC	Fourier ring correlation
SSIM	structural similarity
TIP4A	tangential iterative projections algorithm for anisoplanatic aberrations with adaptive limited support